CHAPTER 9

DEVELOPMENT OF ELECTROMAGNETIC WARMING TECHNOLOGY FOR CRYOPRESERVATION

Ziyuan Wang,[1] Zhiquan Shu,[1,2] Shen Ren,[1,3] Ruidong Ma,[1] John C. Kramlich,[1] Ming Chen,[1] & Dayong Gao[1,*]

[1] Department of Mechanical Engineering, University of Washington, Seattle, WA
[2] School of Engineering and Technology, University of Washington Tacoma, Tacoma, WA
[3] Department of Mechanical Engineering, Seattle University, Seattle, WA

[*] Address all correspondence to: Dayong Gao, E-mail: dayong@uw.edu

Cryopreservation and biobanking of biomaterials (e.g., cells and tissues) plays a critical role in biomedical research, cellular and gene therapy, organ transplantation, tissue engineering, regenerative medicine, new drug/vaccine development, disease screening, clinical diagnostics, in vitro fertilization, conservation of endangered species, etc. However, cryopreservation is facing a big challenge, that the current rewarming process of cryopreserved biomaterials can cause lethal ice recrystallization (IRC) and thermal stress-induced fracture (TSF), damaging living cells and tissues. To prevent both IRC and TSF, a rapid-and-uniform rewarming process is required. However, conventional warming approaches, such as using a stirred warm-water bath, have failed in achieving rapid-and-uniform rewarming. Most recently, new electromagnetic (EM) heating technologies have been developed to achieve rapid-and-uniform rewarming. The EM heating utilizes the phenomenon that dipolar water molecules and cryoprotective agents become excited when exposed to megahertz oscillating EM fields, generating rapid and uniform heating. This chapter introduces the study of the new EM heating technology, including the development of EM resonance cavity, characterization and selection of optimal cryoprotective solutions coupled with EM rewarming, optimization of EM system operation and control, and magnetic-nanoparticle–enhanced EM heating strategy.

KEY WORDS: *dielectric heating, fast and uniform rewarming, cryopreservation, electromagnetic resonance cavity, magnetic nanoparticles*

1. INTRODUCTION

Low temperature has been utilized for long-term cryopreservation of biological materials, such as living cells, tissues, and organs. This is because biochemical reaction rate dramatically diminishes at low temperatures, keeping cells and tissues dormant but potentially alive. Currently, cryopreservation of larger tissues and organs is less successful than that of small samples of a single cell type. This is largely because the optimal cryopreservation conditions, which were developed to prevent cryoinjury caused by lethal intracellular ice formation (IIF) and serious cell dehydration (SCD), are cell-type specific and not appropriate for the cryopreservation of tissues or organs that contain different cell types and a large volume of complicated intercellular matrix, etc.[1,2] To prevent IIF and SCD, vitrification

ISSN: 1049–0787; ISBN: 978–1–56700–547–9/24/$35.00 + $00.00

NOMENCLATURE

C_p	specific heat capacity, J kg^{-1} °C^{-1}
E	electric field strength, V m^{-1}
f_o	resonant frequency of the empty chamber, Hz
K	shape factor
k	thermal conductivity, W m^{-1} °C^{-1}
Q_0	quality factor of the empty chamber
q_{DH}	power density per unit volume, W m^{-3}
T	temperature, °C
t	time, s
V_s	volume of the sample, m^3
Greek Symbols	
ϵ_0	permittivity of vacuum, 8.854×10^{-12} F m^{-1}
ε_r'	relative dielectric constant
ε_r''	relative dielectric loss
ρ	density, kg m^3
ω	angular frequency, s^{-1}
$\tilde{\omega}$	complex angular frequency

(i.e., ice crystal-free cryopreservation) approaches have been successfully developed.[1,2] Vitrification is an amorphous glassy state of matter (e.g., water). To achieve and maintain the vitrification during cryopreservation processes, both cooling and warming rates must exceed the critical cooling rate (CCR) and critical warming rate (CWR) of the specific vitrification solutions and/or vitrified biomaterials during the cooling and rewarming processes, respectively.[3]

Conventional cooling approaches, such as using a controlled-rate freezer, can readily achieve CCR to make biospecimen vitrified. However, a critical problem arises in the rewarming process, i.e., the CWR is too high to be achieved by conventional warming approaches, especially for the rewarming of relatively lager biospecimens. (Note: the CWR is usually much higher than the CCR for the same biospecimen.[3]) Rewarming rates lower than CWR can cause the deadly ice-recrystallization (IRC) in cells and tissues. In addition, conventional rewarming processes are currently conducted by thermal conduction or convection at biospecimen's boundary surfaces, which cause nonuniform warming inside the biospecimen, generating a large temperature gradient, high thermal stress, and biospecimen fracture. Therefore, a rapid-and-uniform warming approach needs to be developed to prevent both IRC and thermal stress-induced fracture (TSF) during the rewarming process.

Electromagnetic (EM) heating, characterized by its potential volumetric heating capability, has been proposed as a promising solution for the rapid-and-uniform rewarming of cryopreserved biomaterials. Two new EM warming approaches have been recently developed to prevent cryoinjury caused by lethal IRC and TSF. One is named "nanowarming" (NW), which employs the hundreds of kHz radiofrequency magnetic field to excite magnetic nanoparticles (NPs) to generate heat. Magnetic NPs are necessary for this method because biological samples themselves lack magnetic properties and cannot be excited by alternating magnetic fields. The NW technology has been successfully applied for the rewarming of rats' organs, including kidneys, hearts, and livers, etc.[4–6] Han et al.[4]

utilized the NW to rewarm vitrified rat kidneys and made successful kidney transplantation.

Another EM heating technology, named "single mode electromagnetic resonance" (SMER), has been developed and applied for the rewarming. Unlike the NW approach, which utilizes magnetic fields and NPs, the SMER heating—a process also known as dielectric heating—applies MHz electric fields to excite dipolar molecules (e.g., water and some cryoprotective agents inside the cryopreserved biospecimen) to fast rotate and align with rapidly alternating-oscillating electric fields, thereby effectively converting electromagnetic energy into thermal energy (i.e., heat). A major advantage of the SMER heating is its unique potential and ability to heat cryopreserved biospecimens/systems that contain a large amount of dipolar water molecules and dipolar cryoprotective agents (CPAs), to achieve rapid-and-uniform rewarming through dielectric heating. The comparison of two methods is provided in Table 1.

This chapter provides an in-depth introduction of the study on scientific mechanisms underlying electromagnetic heating and focuses on the innovative SMER technology, including Maxwell electromagnetic theory, development of the SMER cavity and its control system, characterization and selection of cryoprotective solutions coupled with SMER rewarming, potential magnetic-nanoparticle–enhanced SMER heating strategy, as well as theoretical/numerical and experimental research results for SMER warming optimization and applications.

2. ELECTROMAGNETIC HEATING BACKGROUND AND ADVANCEMENT

The discovery of the electromagnetic heating effect was serendipitous, made by Percy LeBaron Spencer, an American engineer and inventor, in 1945 at the Raytheon Company. During his work on radar technologies, he observed a chocolate bar melting in his pocket. Microwave electromagnetic waves with frequencies between 0.3 and 300 GHz and wavelengths from 1 m to 1 mm occupy the spectrum between radio frequencies and infrared.

TABLE 1: A comparison of nanowarming and SMER warming approaches

Rewarming method	EM wave frequency	Major heating mechanism	EM heating fields	Requirement for MNPs
Nanowarming	1 kHz–1 MHz	Induction heating	Magnetic field	Yes
SMER warming	100 MHz–1 GHz	Dielectric heating in a closed EM resonance cavity	Electric field	No (Note: NPs may also be used in thr SMER warming process to utilize the magnetic field and further enhance the warming rate and uniformity.)

Since then, the commercial microwave oven was introduced and became one of the necessary household appliances.

Electromagnetic heating, in contrast to conductive or convective heating, can thaw a sample volumetrically. This method capitalizes on the inherent electrical properties of the biological materials and CPAs, facilitating a more direct and efficient heating process without the need for additional materials to mediate the energy conversion. The EM heating occurs when high-frequency electromagnetic radiation stimulates the oscillation and rotation of dipolar molecules [e.g., water molecules and some dipolar CPA molecules (e.g., DMSO and glycerol, etc.)] in the biomaterials and surrounding media, converting the electromagnetic energy into thermal energy (heat) through the friction among the rotating and moving molecules. The generated power density per unit volume, q_{DH}, is governed by the following:[7]

$$q_{\mathrm{DH}} = \omega \cdot \varepsilon_r'' \cdot \varepsilon_0 \cdot E^2 \tag{1}$$

where ω is the angular frequency of alternating electric field, ε_r'' is the relative dielectric loss of the heated material, ϵ_0 is the permittivity of vacuum, and E is the electric field strength.

Research into EM heating dates back to the 1960s, with Allen and Ketterer[8] identifying the significant impact of tissue electrical conductivity at varying temperatures on electromagnetic thawing outcomes. In 1970s, Ketterer et al.[9] rewarmed canine kidneys, employing power control to avoid overheating, and claimed partial success in $\sim$ 20 kidneys. In 1977, Guttman et al.[10] achieved electromagnetic rewarming of dog kidneys using a 1.35 kW Toshiba commercial microwave oven at 2.45 GHz, with half of the transplanted dogs surviving 2–14 months after 16 kidneys were frozen to –80°C and then rewarmed. Pegg et al.'s attempts to replicate Guttman's experiment with 14 dog kidneys resulted in no preserved biological functionality post-transplantation using a similar 2.45 GHz microwave.[11] In 1978, Burdette et al.[12] explored an electromagnetic illumination system capable of monitoring power and operating at single or multi-frequency, presenting rewarming results for rabbit and dog kidneys without functional analysis through transplantation. The primary issue with these initial studies was the use of microwaves at frequencies too high for uniform heating of large samples, such as canine kidneys. Better uniformity is achievable with lower frequency of electromagnetic waves since they offer greater penetration depth for the same materials.[13] Additionally, commercial microwave ovens, which are multimode EM cavities, had noncontrollable and nonuniform electromagnetic field distribution inside the ovens, which caused relatively low heating rates and nonuniform heating due to the scattered energy and unpredictable electromagnetic field distribution.

Scientists have tried to develop an EM resonant cavity with multimodes. In the Rachman et al.[14] EM resonance cavity rewarming system, two resonant states (TE111 and TM010) were excited. Similarly, Robinson and Pegg[15] designed another multimode cavity system that excited three distinct modes. These multimode cavities demonstrated superior heating performance compared to commercial microwave ovens. However, advancements were hindered by the difficulties in tracking the resonant state during heating, because of the multimode design and multiple EM input ports compounding the challenge of resonance tracking.

3. OVERVIEW OF SMER WARMING TECHNOLOGY

During the past 25 years, development and optimization of SMER technology has been conducted and advanced continuously.[16–21] This innovative technology resolved prior challenges in multimode EM heating through the design of a new SMER cavity and a resonance tracking system. In addition, characterizing the crucial physical properties of CPA solutions and conducting computer simulations have provided valuable insights for optimizing the SMER heating system. Recently, SMER has been successfully applied to rewarm larger volumes of cryopreserved cell suspensions and tissues, with high post-thaw viability and functional survival of the cells and tissues.[16–21]

3.1 SMER Cavity

Instead of using the multimode resonant cavity, SMER rewarming system takes the single-mode resonant cavity as the applicator.[17] One of the major advantages of the single mode is its more controllable and predictable electromagnetic field, a single-standing EM wave distribution inside the EM resonant cavity. TE101 mode was selected as the single mode, generating in the resonant cavity because this mode features a strong standing wave (electric field) at the center region of the cavity. Considering the EM field intensity distribution uniformity, the penetration depth of the EM wave, and the size of human organs, 434 MHz was selected as the microwave frequency for use in the rewarming of relatively large volumes of cell suspension, tissues, and organs.[15] The resonant cavity was designed as cuboid since it is easier to manufacture in comparison to the cylindrical cavity. From the Luo et al. design,[17] as shown in Fig. 1, a probe antenna is placed at the cavity wall to excite the electric field. The cavity also includes a cooling component, allowing a sample to be cooled inside the cavity. A thermal insulated hollow Styrofoam cylinder is placed at the

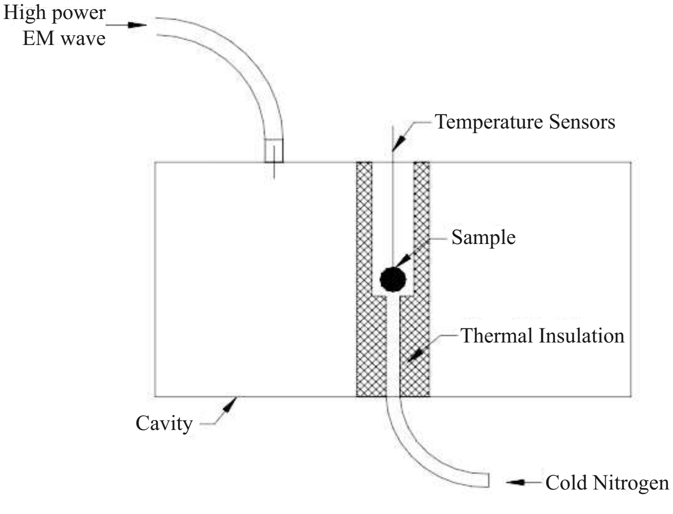

FIG. 1: Schematic of the SMER cavity and cooling component/subsystem (Reprinted with permission from Elsevier, Copyright 2006)[17]

center of the cavity to hold the sample. The sample can be cooled by cold nitrogen gas passing through the hollow cylinder before SMER rewarming starts.

3.2 Microwave Supply

The microwave power is delivered to the resonant cavity to rewarm the cryopreserved biomaterial. A microwave signal is generated by a signal generator. Compared to the traditional magnetron, the signal generator can generate signals with wider frequency range, and it is able to tune the frequency precisely. However, the signal sent by the signal generator has very low power, normally < 1 W. Therefore, a power amplifier always cooperates with the signal generator to achieve a much higher EM power with the desired frequency.

3.3 EM Resonance Tracking

The SMER cavity coupled with a specific EM resonant frequency was initially designed based on the assumption that the cavity has an empty space without samples inside the cavity. However, replacement of a sample/biospecimen into the cavity alters the cavity boundary conditions and dielectric properties, thereby changing the resonant frequency. In addition, the resonance frequency will be changed quickly and continuously during the EM heating process due to the temperature dependance of the permittivity of a sample. This requires adjusting the input microwave frequency simultaneously and continuously to meet the corresponding resonant frequency. Crucially, if the cavity is not in a resonant state, a large amount of EM power will be reflected back to the probe and signal generator, posing potential safety risks to both equipment and people.

To address this big challenge, an automatic monitoring-feedback control system that can collect the EM resonance status information inside the cavity throughout the heating process was invented and developed. This monitoring system also incorporates two fiber-optic temperature sensors to monitor both the rate and uniformity of heating. A spectrum analyzer is used to assess the power reflected at specific frequencies. The gathered data are then fed into a control program, which determines whether the microwave remains in resonance within the cavity and decides on subsequent adjustments to the input microwave frequency. The real-time resonant frequency is determined by evaluating the entire spectrum of reflected power and looking for the lowest power peak. The frequency corresponding to the lowest power peak is the real-time resonant frequency, and the signal generator is dynamically and simultaneously sending the signal with that resonant frequency to maintain EM resonance status during the heating process.

4. DETERMINATION OF PHYSICAL PROPERTIES OF CPA SOLUTIONS

4.1 Dielectric Properties

The interaction between an applied electromagnetic field and biomaterials, which is crucial for determining the absorption of electromagnetic energy by the biomaterials, is characterized by their dielectric properties.[22,23] These properties, which are temperature-dependent, play a significant role in heating efficiency. For an example, the so-called "thermal runaway" phenomenon may occur, i.e., the warmer regions in a biomaterial may absorb more EM energy to convert to heat, leading to increased temperature gradients and thermal stresses, potentially compromising the viability and functionality of cryopreserved materials, especially for larger tissues and organs.[24,25] Understanding the dielectric properties of biomaterials is essential, particularly in cryopreservation and vitrification processes where CPA or vitrification solutions largely determine the overall properties of cell suspensions or tissues. Identifying these properties is crucial for optimizing electromagnetic rewarming strategies.

Determining the dielectric properties of biomaterials necessitates sophisticated sensing and monitoring technologies. A diverse set of measurement techniques, such as transmission and reflection methods, have traditionally been utilized across biomedical applications to assess these properties.[26–28] Typically, these approaches require that samples maintain their structural integrity without any morphological alterations. However, in the context of electromagnetic rewarming, accurately measuring dielectric properties demands conducting assessments at subzero temperatures, a condition that could induce phase changes in the material, thereby rendering traditional transmission and reflection methods unsuitable. The cavity perturbation method is widely utilized to measure the electrical properties of various materials, due to its efficacy in assessing the dielectric properties of low-loss dielectric materials. This method is particularly valuable in the subzero temperature range, where the dielectric properties of biomaterials and CPA/vitrification solutions are normally very small. Consequently, cavity perturbation is employed to measure the dielectric properties of CPA/vitrification solutions at temperatures of $< 0°\mathrm{C}$.

4.1.1 Cavity Perturbation Theory

The theoretical derivation of cavity perturbation theory starts with the equations, as follows:[29]

$$\frac{\Delta\tilde{\omega}}{\tilde{\omega}} = \frac{\Delta f}{f_0} + \frac{1}{2}\left(\frac{1}{Q} - \frac{1}{Q_0}\right) \tag{2}$$

$$\frac{\Delta\tilde{\omega}}{\tilde{\omega}} = \frac{\int_{V_s}\left(\Delta\varepsilon\vec{E}\cdot\vec{E}_0^* + \Delta\mu\vec{H}\cdot\vec{H}_0^*\right)dV}{\int_{V_c}\left(\varepsilon\vec{E}\cdot\vec{E}_0^* + \mu\vec{H}\cdot\vec{H}_0^*\right)dV} \tag{3}$$

where $\tilde{\omega}$ is the complex angular frequency of the cavity, f_0 is the resonant frequency of the empty chamber, Q_0 is the quality factor of the empty chamber, V_s is the volume of the sample, V_c is the volume of the chamber, $\vec{E}_0$ and $\vec{H}_0$ are electric and magnetic fields inside the empty chamber, $\vec{E}$ and $\vec{B}$ represent electric and magnetic fields inside the chamber with the sample added, ε and μ are complex permittivity and permeability of the sample, and i is the imaginary number. For a nonmagnetic sample, μ is equivalent to the permeability of free space μ_0. Then, Eq. (3) can be simplified as follows:

$$\frac{\Delta\tilde{\omega}}{\tilde{\omega}} = -(\varepsilon_r - 1)\frac{\int_{V_s} \vec{E}_{\text{int}} \cdot \vec{E}_0^* dV}{2\int_{V_c} \left|\vec{E}_0\right|^2 dV} \tag{4}$$

$$\varepsilon_r = \varepsilon_r' - i\varepsilon_r'' \tag{5}$$

where $\vec{E}_{\text{int}}$ stands for the incident electric field within the sample; ε_r is the relative permittivity of material and is calculated by the permittivity ε divided by the permittivity of the free space ε_0. ε_r' is the real part of the relative permittivity or called the dielectric constant, and ε_r'' is the imaginary part of the relative permittivity or called the dielectric loss. Plug Eq. (5) into Eq. (4),

$$\frac{\Delta\tilde{\omega}}{\tilde{\omega}} = -(\varepsilon_r' - 1)\frac{\int_{V_s} \vec{E}_{\text{int}} \cdot \vec{E}_0^* dV}{2\int_{V_c} \left|\vec{E}_0\right|^2 dV} + i\varepsilon_r''\frac{\int_{V_s} \vec{E}_{\text{int}} \cdot \vec{E}_0^* dV}{2\int_{V_c} \left|\vec{E}_0\right|^2 dV} \tag{6}$$

Comparing Eqs. (2) and (6),

$$\frac{\Delta f}{f_0} = \frac{i}{2}\left(\frac{1}{Q} - \frac{1}{Q_0}\right) = -\left(\frac{1}{C}\right)K(\varepsilon_r' - 1) + i\varepsilon_r''\left(\frac{1}{C}\right)K \tag{7}$$

where C is proportional to

$$\frac{1}{V_s}\int_{V_c} \frac{\left|\vec{E}_0\right|^2}{\left|\vec{E}_{0,\max}\right|^2}$$

and $\vec{E}_{0,\max}$ is the value of the highest electric field intensity that locates at the center position of the rectangular chamber. K is a shape factor that is determined by the geometry of the sample.

Separate Eq. (7) to obtain

$$\Delta f = C_1 K(\varepsilon_r' - 1) \tag{8}$$

$$\Delta\left(\frac{1}{Q}\right) = C_2 K \varepsilon_r'' \tag{9}$$

where C_1 and C_2 are constants. For spherical sample, $K = 3/(\varepsilon_r' + 2)$. Then, Eqs. (8) and (9) become

$$\Delta f = k_1 \frac{\varepsilon_r' - 1}{\varepsilon_r' + 2} \tag{10}$$

$$\Delta\left(\frac{1}{Q}\right) = k_2 \frac{\varepsilon_r''}{(\varepsilon_r' + 2)^2} \tag{11}$$

where Δf represents the difference in resonant frequency of the cavity with and without the sample under test, ε_r' and ε_r'' denote the dielectric constant and loss of the sample, respectively. The $\Delta(1/Q)$ is the change in the reciprocal of the quality factor of the cavity, with and without the sample, and k_1 and k_2 are constants related to the volume and shape of the sample under test.

According to the cavity perturbation theory, this measurement system includes consists of a resonant cavity, network analyzer (E5061B, Agilent Technologies, Santa Clara, CA), temperature meter (ReFlex, Neoptix, Quebec, Canada), and fiber-optic temperature sensor (TS4-02, Micronor LLC, Camarillo, CA), as shown in Fig. 2.

4.1.2 System Calibration

Before applying cavity perturbation theory to assess the dielectric properties of unknown solutions, it is essential to determine two constants, k_1 and k_2, through calibration with standard solutions. The dielectric properties of these standard solutions at room temperature are documented in Table 2.[15] The $\Delta(1/Q)$ and Δf for each standard solution will be determined using a network analyzer. These measurements, alongside the corresponding dielectric properties, will be input into Eqs. (9) and (10) to find k_1 and k_2 through linear fitting, as shown in Fig. 3.

Figure 3(a) shows the change of the resonant frequency before and after the insertion of the standard solutions [plot of Eq. (9)]. Figure 3(b) shows the change of the inverse of

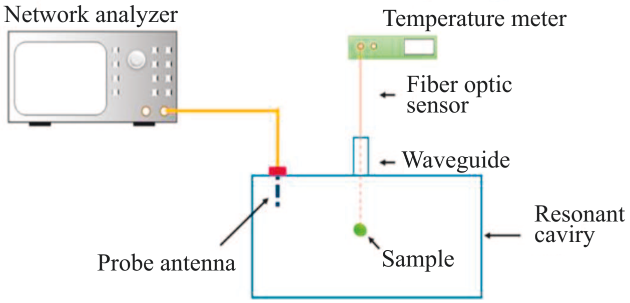

FIG. 2: Diagram of the system for measurement of dielectric properties (Reprinted under a Creative Commons Attribution license, Copyright 2020; https://creativecommons.org/licenses/by/3.0/)[30]

TABLE 2: The dielectric properties of the standard solutions at 20°C and 438 MHz[15]

Solution	Dielectric constant ε_r'	Dielectric loss ε_r''
Water	80	1.9
Methanol	33	3.52
Ethanol	22	7.04
1-Propapnol	13	8.57
2-Propanol	12	8.08
Ethylene glycol	36	12.09
Cyclohexane	2.02	0

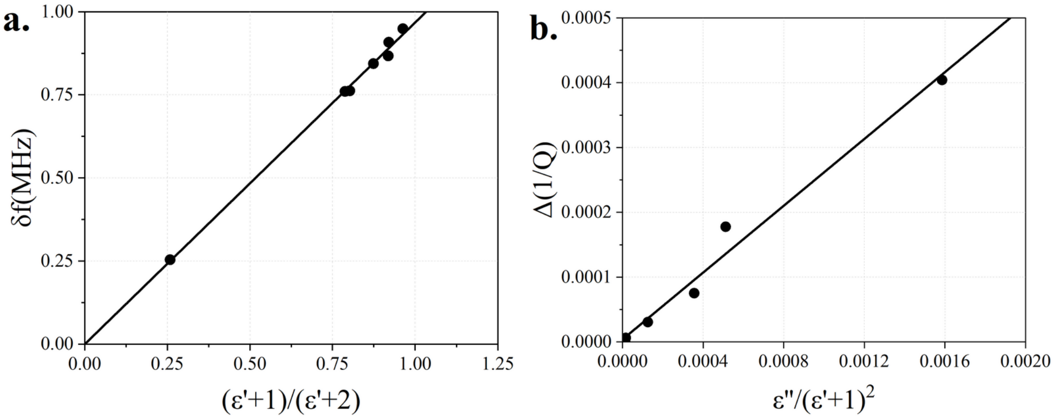

FIG. 3: (a) Resonant frequency shift of the resonant cavity after loading different calibration solutions: water, methanol, ethanol, 1-propanol, 2-propanol, ethylene glycol, and cyclohexane; and (b) Inverse of quality factor change of the resonant cavity after loading different calibration solutions: water, methanol, ethanol, 1-propanol, 2-propanol, ethylene glycol, and cyclohexane (Reprinted with permission from Mary Ann Liebert, Copyright 2017)[31]

the quality factor [plot of Eq. (10)]. The correlation factor R^2 was calculated as 0.9943 for the fitting of the resonant frequency and 0.989 for the inverse of the quality factor to validate the goodness of fit. Then, k_1 and k_2 can be determined from the slope as 0.964 MHz and 0.2826.[31]

Following calibration, the measurement system is equipped to assess the dielectric properties of unknown solutions. On the basis of Eqs. (9) and (10), the dielectric constant and loss can be obtained as follows:

$$\varepsilon_r' = \frac{k_1 + 2\Delta f}{k_1 - \Delta f} \tag{12}$$

$$\varepsilon_r'' = \frac{1}{k_2}(\varepsilon' + 2)^2 \Delta\left(\frac{1}{Q}\right) \tag{13}$$

4.1.3 Dielectric Properties Measurement Results

Measurements have been focused exclusively on vitrification solutions with relatively higher CPA concentrations because low-CPA-concentration solutions, typically utilized for cell cryopreservation with ice formation, exhibit only negligible differences in complex dielectric properties. The selected vitrification solution includes DPVP, EPVP, PPVP, VS55, VS83 and their composition can be found in Table 3.

Dielectric loss ε_r'' characterizes the ability to absorb electromagnetic power. For different CPA solutions, dielectric loss ε_r'' is key in determining how fast the solution could pass through the frozen zone: the larger the dielectric loss is, the more efficient the absorption

TABLE 3: Composition of measured vitrification solutions

	DPVP	EPVP	PPVP	VS55	VS83
DMSO, g	410			242.14	363.21
Ethylene glycol, g		440			
Propylene glycol, g			360	168.38	252.57
PVP, g	60	60	60		
5X Euro Collins, mL				200	200
Formamide, g				139.56	209.34
Euro Collins Solution				To 1 L	To 1 L
PBS	To 1 L	To 1 L	To 1 L		

of electromagnetic energy by the material is, which leads to an increased heating rate. The measured dielectric properties can be found in Fig. 4.[21]

4.2 Determination of Thermal Properties

4.2.1 Measurement of Specific Heat

To determine the temperature-dependent specific heat, differential scanning calorimetry [(DSC) Perkin Elmer DSC 8000] can be used to take accurate measurement of various vitrification solutions. DSC precisely measures the heat flow through the vitrification solution samples. The isothermal step scan method is adopted to minimize experimental errors, as follows:

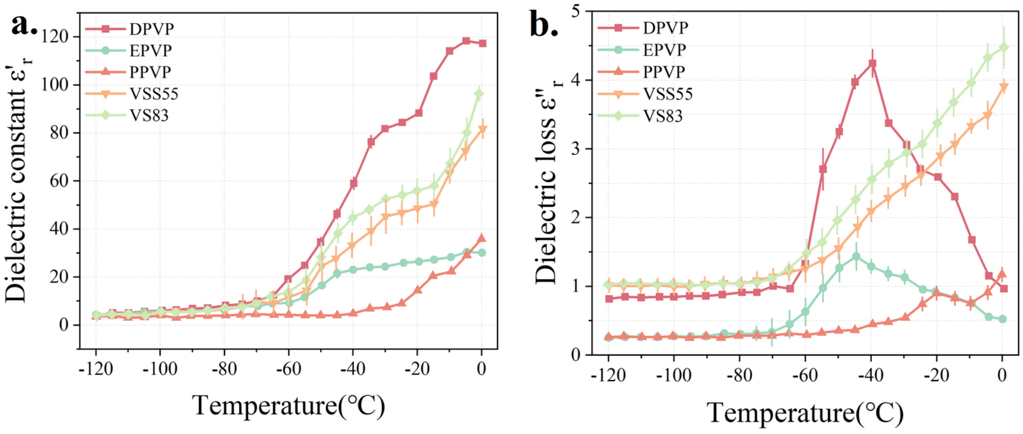

FIG. 4: Dielectric properties of vitrification solutions: (a) ε'_r versus the temperature for DPVP, EPVP, PVP, VS55, and VS83. The mean values ± standard deviations at each temperature point were determined based on four replicates ($n = 4$) and (b) ε''_r versus the temperature for DPVP, EPVP, PVP, VS55, and VS83. The mean values ± standard deviations at each temperature point were determined based on four replicates ($n = 4$).[21]

$$\Delta Q_{\text{DSC}} = C_p m \Delta T \tag{14}$$

ΔQ_{DSC} is the heat flow through the vitrification solution sample, m is the mass of vitrification solution sample, and T is the temperature. The heat flow at each temperature was obtained at cooling and rewarming process. The DSC experiment for each vitrification solution sample was repeated three times (n = 3). The latent heat was incorporated into the effective specific heat capacity when the phase transition occurs.

4.2.2 Measurement of Thermal Conductivity

Thermal conductivity of each of vitrification solutions is measured using a microthermal sensor developed by Liang et al.[32] The sensor works based on the principle of transient hot wire. This miniaturized device utilizes a SiO_2/Au/SiO_2 sandwiched structure to protect the microfabricated serpentine gold coil, which functions as both the heater and a passive thermometer. The sensor was already tested and shown to measure thermal conductivity of biomaterials and solutions with high accuracy, repeatability, and reliability. All experiments were performed more than three times at 20°C.

4.2.3 Thermal Property Measurement Results

After measuring by DSC, the specific heat values of tested vitrification solutions are shown in Fig. 5.[33] The thermal conductivity and density of tested vitrification solutions were measured, and the results are shown in Table 4. The measurements were conducted over a temperature range of –40 to 40°C, revealing a phenomenon: the thermal conductivity value remains relatively constant for solutions with higher DMSO concentrations.[32] This observation aligns with findings from the work of Ehrlich et al.[34] Consequently, we have assumed thermal conductivity to be constant for future simulations and experiments.

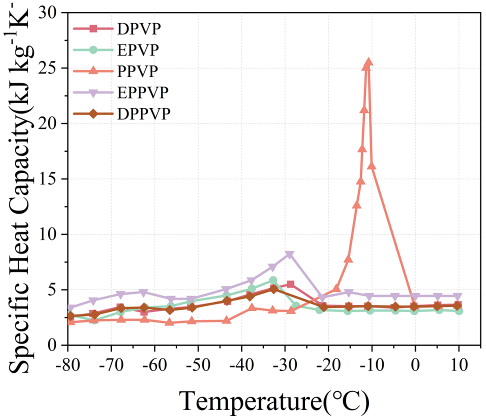

FIG. 5: Specific heat of different kinds of tested vitrification solutions (Reprinted with permission from Elsevier, Copyright 2018)[33]

TABLE 4: Thermal conductivities of vitrification solutions

Solution	Density (g mL^{-1})	Thermal conductivity (W m^{-1} K^{-1})
DPVP	0.92	0.408
EPVP	0.894	0.407
PPVP	0.796	0.454
DPPVP	0.932	0.423
EPPVP	1.018	0.542

4.3 Discussion

In the past, most cryobiological studies focused on the development of new vitrification solutions and their potential side effects, such as effects of high CPA concentrations on the osmotic injuries and chemical toxicity to cells, etc. This section reports the measured physical properties of the vitrification solutions, which may have significant effects on the SMER heating process. This is because the ability of the vitrification solution to absorb electromagnetic energy depends on their dielectric properties. In addition, the SMER heating performance depends on the thermal properties of the CPA/vitrification solution. Therefore, the thermal and dielectric property can be used as additional determinant factors for the development and optimization of the new CPA/vitrification solutions, which not only ensure vitrification during cooling process but also enhance rapid and uniform heating during the SMER rewarming process to prevent lethal ice recrystallization and thermal-stress–induced fracture in the specimens.

Dielectric loss (ε_r'') reflects a material's ability in absorbing electromagnetic power. A higher dielectric loss means more efficient absorption of electromagnetic energy, leading to faster heating rates. Figure 4(b) shows that dielectric loss for all examined CPA solutions remained low below –70°C, suggesting initial slow heating by electromagnetic waves in frozen CPA/vitrification solutions. The measurements indicated negligible variation in dielectric properties below –120°C. As a result, our analysis is concentrated on the temperature range between –120 and 0°C.[35] As temperature rises, dielectric loss for all solutions increases, peaking between –45 and –20°C, then declines with further temperature increase. Specifically, PPVP's dielectric loss increases past its nadir with temperature rise, whereas for DPVP and EPVP, dielectric loss continues to fall within the subzero range until reaching 0°C.

Among the CPA/vitrification solutions studied, DPVP exhibits a higher dielectric loss, suggesting a greater capacity for absorbing electromagnetic energy when exposed to an electric field of the same intensity. The inverted "U" shape observed in the dielectric loss of DPVP and EPVP solutions indicates a decrease in dielectric loss beyond their peak values as temperature increases. Consequently, areas at higher temperatures would experience a slower warming rate, allowing colder regions with relatively higher warming rate to catch up, thereby minimizing temperature differentials within the sample.

In assessing thermal properties, we found no notable differences in the density of various vitrification solutions. For the conventional boundary warming method, such as heating with a water bath, thermal conductivity is crucial for heat transfer via conduction within the sample. Utilizing microelectromechanical system sensors, we determined the thermal conductivity of the CPA solutions under examination (refer to Table 4).

The amount of latent heat may greatly affect the warming rate in the specimen during phase transition. The enthalpy method was employed to model phase-change scenarios. Among the five CPA solutions analyzed, PPVP and EPVP exhibited substantially higher effective specific heats (as shown in Fig. 5), indicating a higher thermal energy requirement for rapid rewarming. Analysis of electric and thermal properties revealed that DPVP possesses a higher capacity to absorb electromagnetic energy, coupled with a relatively lower specific heat (rewarming rate is inversely dependent on specific heat), suggesting it could achieve a faster warming rate in comparison to other CPA solutions.

4.4 Conclusion

This section aimed to identify optimal vitrification solutions for electromagnetic rewarming. A dielectric property measurement system for vitrification solutions and biomaterials was developed by employing the cavity perturbation technique. Calibration showed the resonant cavity's frequency shift and quality factor changes aligned with theoretical predictions. The measurements of several vitrification solutions' dielectric properties at subzero temperatures allowed researchers to calculate penetration depths, which were found to be sufficient for electromagnetic wave propagation and heating. Among the solutions, DPVP emerged as the preferred option for electromagnetic rewarming, attributed to its lower specific heat, higher dielectric loss, and the unique inverted U-shaped curve of its dielectric loss at subzero temperatures. These properties suggest that using DPVP could achieve faster warming rates and mitigate the thermal runaway. Although this investigation concentrated on selecting vitrification solutions for effective and uniform rewarming via electromagnetic heating, the dielectric measurement system designed here can also help pinpoint optimal CPA/vitrification solutions or biomaterials for electromagnetic rewarming in cryopreservation. Furthermore, this system has potential applications in other biomedical fields involving electromagnetic waves, such as microwave-heating hyperthermia therapy or microwave tomographic imaging.

5. NUMERICAL SIMULATION AND OPTIMIZATION OF SMER SYSTEM

Various numerical techniques have been employed to design and optimize electromagnetic rewarming systems, notably: (i) finite difference time domain (FDTD), (ii) method of moment (MOM), and (iii) finite element method (FEM).[36,37] The FDTD method accurately predicts temperature distributions but is resource-intensive due to its fine grid requirement.[38] MOM excels in analyzing homogeneous dielectrics but struggles with complex geometries like single-mode resonant cavities.[36] Simulations involving superparamagnetic NPs faced practical challenges, notably the high power input of 8×10^3 W needed for adequate warming rates.[39] Studies by Ma et al.[40] and Torres et al.[41] utilizing FDTD, and

Pathak et al.'s[42] multi-grid 3D FDTD with heat transfer model, along with Zhang et al.'s[43] 3D model for field and power distribution within microwave cavities, have all contributed to this field.

This section introduced an efficient and effective model using the FEM that integrates electromagnetic wave propagation and the heat transfer process. Numerical optimization was carried out to predict the ideal shape of cryopreserved samples for the rapid and uniform rewarming. Given the pivotal role of CPA solutions in preventing cryoinjuries and their significant influence on the properties of cryopreserved biomaterials, essential physical properties of various CPA solutions (such as complex permittivity, specific heat, and thermal conductivity, characterized experimentally in Section 4) were incorporated into this numerical simulation. Utilizing the numerical model, the optimum CPA solutions were identified for the warming processes. Building on the numerical optimization of sample shape and CPA choice, a conceptual hybrid electromagnetic-conduction heating approach was proposed, experimentally tested, and compared to traditional electromagnetic heating methods. This approach showed promise in reducing the nonuniformity associated with electromagnetic heating. This study offers valuable insights into selecting vitrification solutions and developing electromagnetic rewarming systems, aiming to enhance organ preservation techniques.

5.1 Numerical Simulation Model: Formulation and Validation

5.1.1 Theoretical Formulation

The basic setup of the electromagnetic rewarming system, depicted in Fig. 6, builds upon a previous design. It comprises an electromagnetic signal source and a resonant chamber designed to focus electromagnetic energy at its center, where the cryopreserved materials are heated. Electromagnetic waves are introduced into this rectangular cavity via a coaxial transmission line, with a probe antenna employed to stimulate the electric field, thereby creating a standing wave pattern within the resonant cavity. This arrangement ensures the

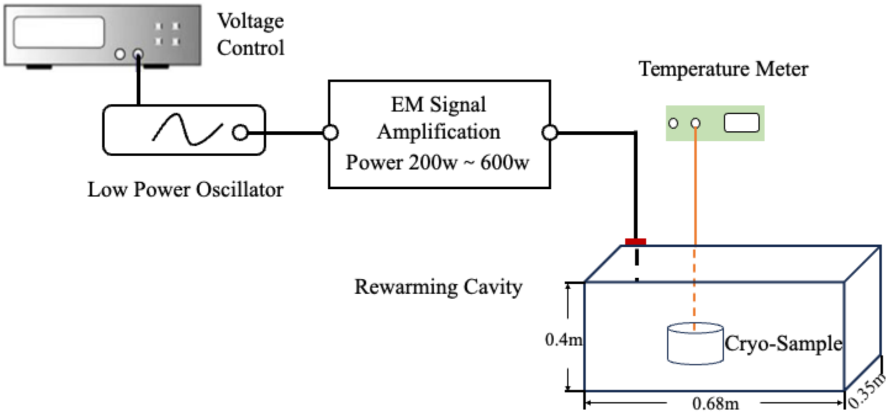

FIG. 6: Schematic of the experimental setup of the electromagnetic rewarming system

highest electric field intensity at the center, precisely where the cryopreserved sample is situated.

For a nonmagnetic material, such as cryopreserved tissue, characterized by its electric parameters including complex electric permittivity (ε, measured in farad per meter), electrical conductivity (σ, measured in siemens per meter), and magnetic permeability [equal to that of free space ($\mu = \mu_0$, measured in henries per meter)]. The distribution of the electric field within the material can be ascertained by solving the following frequency-domain Maxwell equations:

$$\nabla \times \vec{E} = -j\omega\mu\vec{H} - \vec{M} \tag{15}$$

$$\nabla \times \vec{H} = j\omega\varepsilon\vec{E} + \sigma\vec{E} + \vec{J} \tag{16}$$

where $\vec{E}$ (measured in volt per meter) and $\vec{H}$ (measured in ampere per meter) are the electric field and magnetic field components. $\vec{M}$ (measured in ampere per meter) and $\vec{J}$ (measured in ampere per meter square) are the equivalent primary sources, which can be omitted because no magnetic or electrical current source exists in the domain, and ω is the angular frequency of the EM field.

The complex electric permittivity is $\varepsilon_r = \varepsilon_r' - i\varepsilon_r''$. The real part ε_r', also known as dielectric constant, represents the ability of storing electric field energy. The imaginary part ε_r'', known as dielectric loss, represents the ability to absorb electric field energy and convert to heat. This energy absorption or dielectric heating is due to the vibration of molecular dipoles under the influence of electromagnetic field. The generated power density per volume q_{DH} is governed by the following:[44]

$$q_{\mathrm{DH}} = \pi \cdot f \cdot \varepsilon_r'' \cdot \varepsilon_0 \cdot E^2 \tag{17}$$

where f is the frequency of alternating electric field, ε_r'' is the relative dielectric loss of the heated material, ε_0 is the permittivity of vacuum, E is the electric field strength, and q_{DH}, the total absorbed power from the electromagnetic field, can be combined into the heat transfer equation as the heat source term, as follows:[45]

$$\rho C \frac{\partial T}{\partial t} = \nabla \cdot (k\nabla T) + q_{\mathrm{DH}} \tag{18}$$

where ρ denotes the density of the cryopreserved material, C stands for specific heat, k is thermal conductivity, T is the temperature of the material, and t is time.

In this numerical analysis, the properties of the cryopreserved material were defined to vary with temperature, as determined by experimental data. Following the calculation of temperature distribution, thermal and electrical properties were updated to reflect these changes. Consequently, the electromagnetic field distribution was modified in response to the adjustments in material parameters due to temperature changes. The heating source was then recalibrated based on the applied electromagnetic field and the sample's dielectric loss (ε_r''). Thus, temperature and electromagnetic fields were interlinked in this model. Boundary conditions for the sample were set to adiabatic, eliminating the effects of natural convection. Additionally, the resonance chamber's inner wall was treated as a perfect conductor ($\vec{n} \times \vec{E} = 0$, where $\vec{n}$ is the unit vector normal to the cavity's inner surface).

5.1.2 Numerical Model Setup

Applying the FEM, the numerical modeling of the electromagnetic resonant rewarming was accomplished with COMSOL Multiphysics (COMSOL Inc., Burlington, MA). As shown in Fig. 7, the model of the rewarming system consists of the resonant cavity, electromagnetic power input, coaxial transmission line, probe antenna, and cryopreserved sample solution. Table 5 presents the dimension and physical properties of the rewarming system.[33]

To ensure accuracy in the simulation, the Nyquist criterion was utilized for meshing, setting the maximum grid element size to be less than half the electromagnetic wave's wavelength. To further refine the solution of Maxwell's equations, six grids per wavelength were implemented in the finite element analysis.[46] Tetrahedral grids were chosen for their smaller size relative to the discretization required for the resonant rewarming system, ensuring the grid size within the resonant chamber was $< 10\%$ of the electromagnetic wave's wavelength. As depicted in Fig. 8, various meshing strategies were applied to

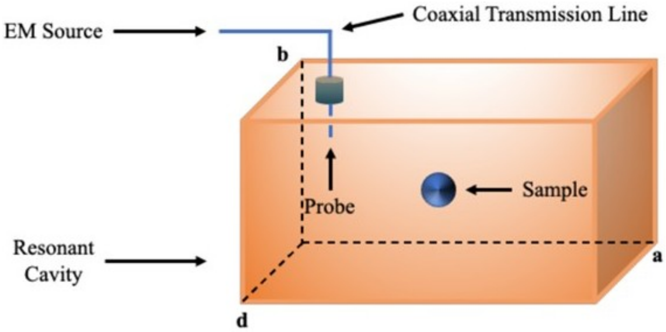

FIG. 7: Schematic of the simulated electromagnetic resonant rewarming system. The dimensions of the cavity are provided in Table 5.

TABLE 5: Geometry and material properties of the cavity system

Parameters	Value
Length of the cavity, mm	680
Width of the cavity, mm	400
Height of the cavity, mm	350
Probe antenna length, mm	40
Probe antenna radius, mm	1.5
Coaxial transmission line impedance, Ω	50
Power input, W	400
Electrical conductivity of copper, S m^{-1}	5.59×10^7
Relative permittivity of air	1
Electrical conductivity of air, S m^{-1}	0

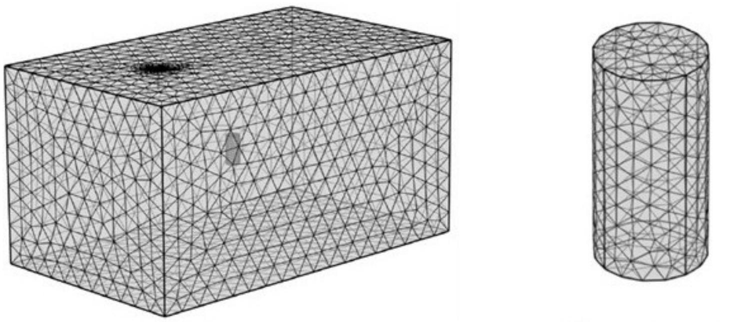

(A) Cavity (B) Sample Holder

FIG. 8: Meshed computation model of the resonant cavity and sample holder. The dimensions of the cavity are provided in Table 5.

different system components, with refined meshes near surface boundaries and enhanced meshing around the probe antenna and the central area of the sample holder.

5.1.3 Numerical Simulation Validation

The numerical model underwent a validation process, by comparing the computed numerical results to the analytical solution at resonant frequency of 434.767 MHz. Numerical results for the normalized electric field distribution within the resonant cavity were plotted alongside the analytical solution (see Fig. 9), showing strong concordance between the two sets of results. The electric field intensity within the cavity/chamber was observed to increase quickly toward the center of the cavity, where cryopreserved samples are located. This suggests that electromagnetic energy is concentrated at the center, allowing for highly efficient utilization in a resonant state.

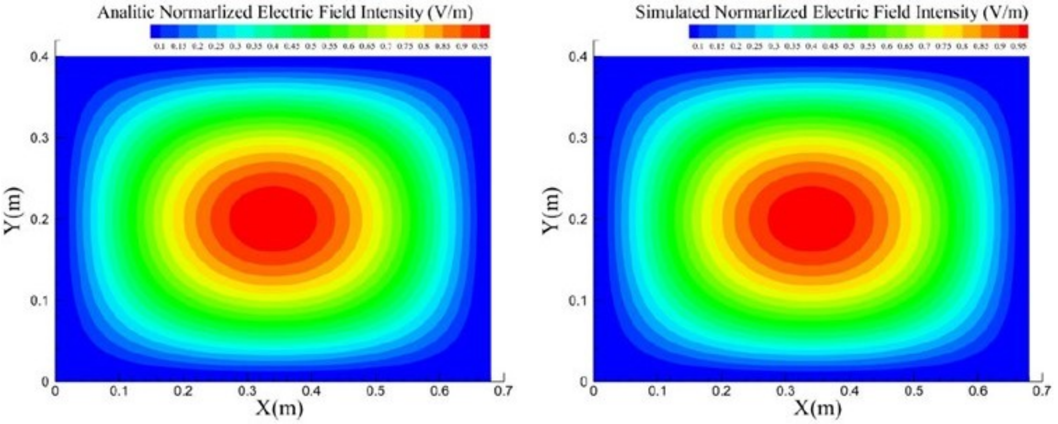

FIG. 9: Distribution of the electrical field magnitude at the central cross-sectional plane in the electromagnetic rewarming chamber (top view). Analytical and simulated results show that electric field energy is concentrated in the center region of the cavity.

In addition to comparing the electric field intensity, the numerical simulation of rewarming 25 mL of 50% DMSO solution from –80 to 0°C was performed to validate the coupled electromagnetic heat transfer process. The configurations of the simulation, including the onset rewarming temperature, applied electromagnetic frequency (∼ 430 MHz), and 400 W source power input, were consistent with the previous experimental study.[17] Before performing the numerical simulation, physical properties were determined. The thermal conductivity k was 0.468 W m^{-1}, K^{-1} and the density was 1.056 g mL^{-1} at room temperature. Both were set as constants in the numerical simulation.

Figures 10(a) and 10(b) show the complex permittivity and specific heat of 50% DMSO solution in the subzero temperature range, which were used in numerical simulation. The simulated warming process demonstrated the same trend with the experimental result as shown in Fig. 11. The consistency between the numerical simulation and experimental

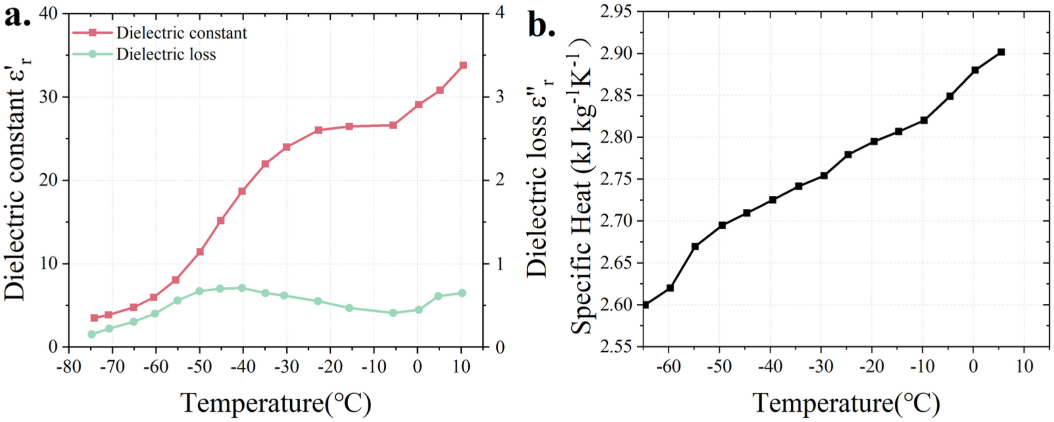

FIG. 10: (a) Complex electric permittivity of 50% DMSO solution and (b) specific heat of 50% DMSO solution

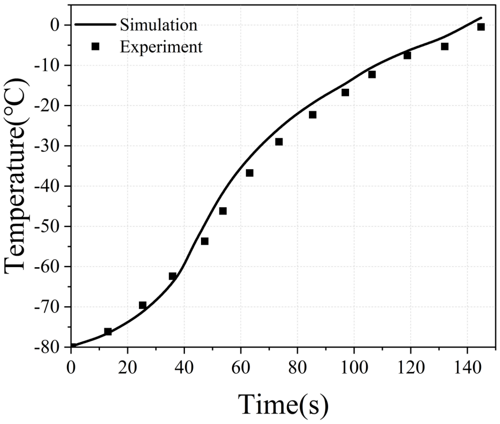

FIG. 11: Validation of the model by comparing the experimental result (black squares) and simulated result (gray line) of electromagnetic heating of 50% DMSO solution

heating results confirmed the reliability of this numerical model. In the numerical simulation, the resonant cavity, which converts electromagnetic energy into heat, was assumed to be an ideal resonator. Thus, the slightly lower warming rate (2.5% difference) in the experiment may be due to the imperfect manufactured resonant chamber with undermined electromagnetic energy conversion ability.

Caution should be exercised in the manufacturing of the electromagnetic resonant chamber. Electromagnetic energy leakage should be restricted to avoid decelerating the warming rate. Most electromagnetic rewarming experimental platforms used temperature sensors (72, 76, 90, 91) penetrating the cavity to monitor the real-time inside temperature of the cryopreserved material, which could lower the efficiency of the heating cavity.[15,47,48] With an extensive temperature profile obtained by the numerical models, the number of sensors used in the experimental platforms may be reduced.

5.2 Effect of Sample Shape on SMER Rewarming

Exploring the optimal sample shape for SMER rewarming is crucial to minimize thermal stresses generated from nonuniform heating and to optimize the electromagnetic field patterns tailored to specific shapes of cryopreserved materials. Given the challenge of both analytically studying complex interactions and accurately monitoring temperatures experimentally, this numerical study compared only four different sample shapes including cylindrical, ellipsoidal, spherical, and cubic (with dimensions detailed in Table 6) and each sample has an identical volume of 24.4 mL. This study aimed to assess the impact of sample shape on rewarming efficiency. As temperature increased from –80 to 0°C, as depicted in Fig. 12, the average warming rates observed for cylindrical, ellipsoidal, spherical, and cubic shapes were 70.5, 61.2, 43.6, and 24.1°C/min, respectively. The average rewarming rate was calculated as the difference between the initial temperature and final temperature, divided by the time. The results indicate that cylindrical and ellipsoidal shapes are beneficial for achieving higher warming rates.[33]

The post-thawing temperature profile was evaluated (Fig. 13). The temperature gradients, defined as the difference between the maximum and minimum temperatures in the sample divided by the distance between them, for cylindrical, ellipsoidal, spherical, and

TABLE 6: Dimensions of sample holder shapes

Parameters	Value (mm)
Radius of sphere	18
Radius of cylinder	18
Height of cylinder	20
a-semi axis of ellipsoid	23
b-semi axis of ellipsoid	14
c-semi axis of ellipsoid	18
Side length of cube	29

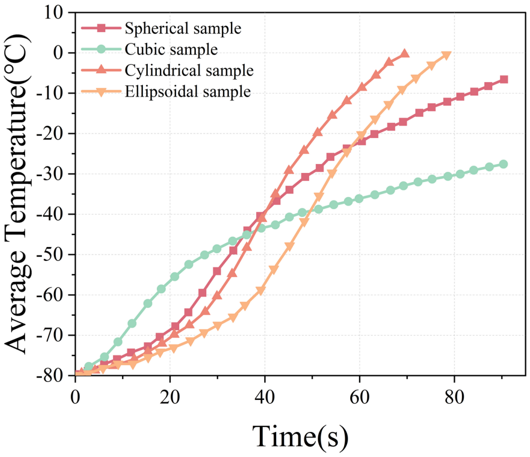

FIG. 12: Simulated SMER rewarming of cryopreserved DMSO solution in different sample holder shapes—the cubic sample was rewarmed at a slowest rate while the cylindrical was the fastest

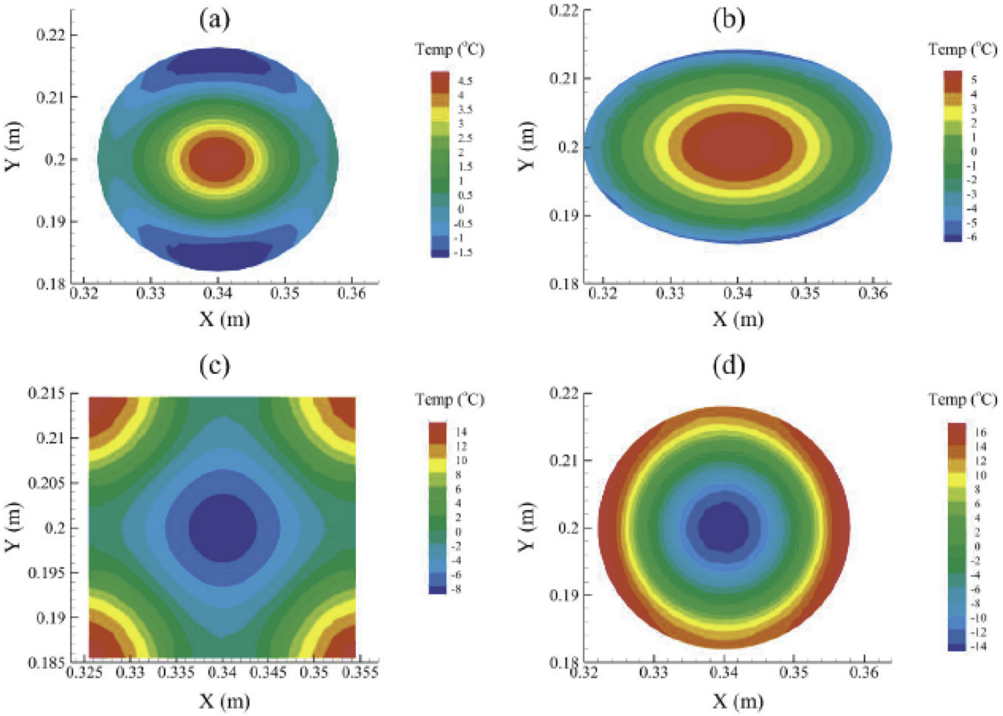

FIG. 13: Simulated post-thawing temperature distribution of cryopreserved DMSO solution in different sample holder shapes: (a) spherical shape, (b) ellipsoidal shape, (c) cubic shape, and (d) cylindrical shape. (The dimensions of the holders are provided in Table 6.) The spherical and ellipsoidal samples manifested more uniform temperature distribution than cubic and cylindrical samples.

cubic samples, were 1.67, 0.78, 0.33, and 1.5°C/mm, respectively. The cubic sample not only could hardly be rewarmed rapidly, but the final temperature distribution was also excessively nonuniform, which confirmed that samples with sharp edges were not appropriate to be rewarmed by the electromagnetic rewarming technique.[22,49]

In contrast, ellipsoidal samples could be rewarmed at a relatively high warming rate, which is consistent with Robinson et al.'s assumption[22] that ellipsoidal sample shape was more appropriate for electromagnetic rewarming based on his investigation using a cone-shape sample holder to imitate ellipsoid. The current simulation results affirmed the relative rapidity and uniformity of ellipsoidal sample shape for electromagnetic rewarming. However, difficulties in manufacturing likely inhibit the adoption of the ellipsoidal or spherical sample shapes. Cryopreserved materials must be placed in the optimal sample holders. The sample holder should be made of a thin-layer material with minimal electromagnetic absorption. It is challenging to make such a holder with desired dimensions for spherical or ellipsoidal shape. In addition, extra support is needed to fix the ellipsoidal sample at the position to be rewarmed rapidly, which can in turn result in the change of electromagnetic field distribution. In contrast, using a cylindrical sample holder can not only avoid these problems but also is beneficial for rapid SMER rewarming (Fig. 12). Therefore, in Section 5.3, the cylindrical sample shape is chosen in the investigation. A hybrid warming strategy was evaluated experimentally to improve rapid and uniform rewarming of cylindrical samples or samples in cylindrical holders.

5.3 Warming Uniformity Improvement by a Hybrid Rewarming Approach

As discussed earlier, the rewarming rate of cylindrical-shape sample is high, but the temperature distribution is relatively nonuniform. To achieve uniform warming, a hypothetical hybrid rewarming concept was evaluated and tested experimentally by inserting an auxiliary rod in the cylindrical sample holder as a passive heating source to reduce the temperature difference between the inner part and boundary of the cryopreserved sample during the SMER rewarming process. On the basis of previous simulated rewarming results of CPA solutions, DPVP was used as the CPA solution sample to be rewarmed in the hybrid rewarming investigation.

For the SMER rewarming experiments with or without the embedded central heating rod, temperature changes at two positions were monitored. One sensor was placed at the center of the sample, and another sensor was placed at a position 10 mm away from the center [Fig. 14(a)]. As illustrated in Fig. 14(b), using the cylindrical sample holder generated a temperature difference of > 20°C between the two monitoring positions with using SMER only. The hybrid rewarming method using both SMER and the central heating rod yielded faster rewarming rates, and the temperature difference between two monitoring positions was reduced to < 10°C. The corresponding temperature gradient (temperature difference divided by the distance) was greatly improved from > 2°C/min (SMER warming only) < 1°C/min (hybrid warming). Aside from this, this temperature gradient was minimized toward the end of the rewarming process using the hybrid rewarming method, which indicated the thermal runaway phenomenon was inhibited using the hybrid method

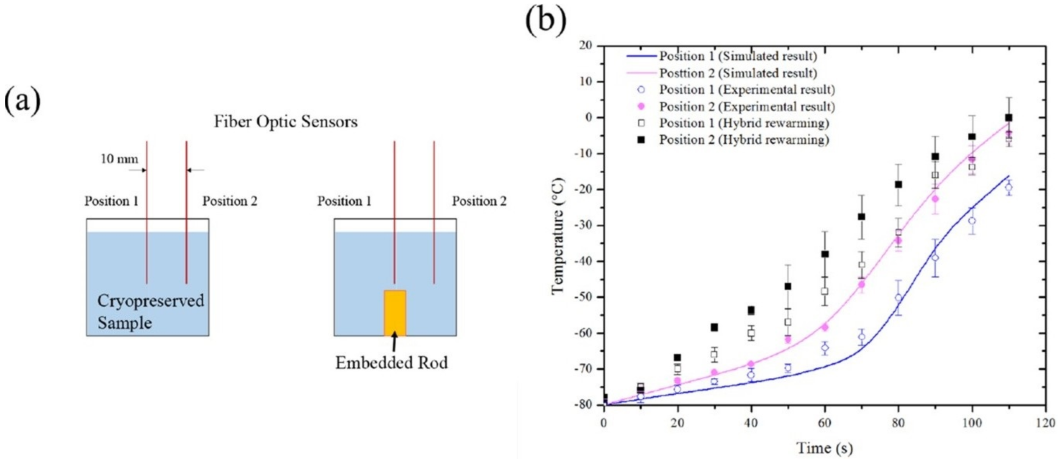

FIG. 14: (a) Illustration of temperature sampling positions. (b) Rewarming results of DPVP. Lines represent the temperature at two positions from numerical simulation. The experimental temperature change at the two positions during the rewarming are denoted by hollow circles and solid circles. Solid and hollow squares represent the temperature change by SMER + heat conduction hybrid rewarming approach.

coupled with the CPA solution. In contrast, the temperature gradient would keep increasing toward the end of the rewarming process if only SMER was used.

5.4 Discussion and Conclusion

The temperature profile during rewarming is crucial for assessing the SMER rewarming system's effectiveness and for designing more efficient systems. Experimentally measuring temperature distribution often involves a trade-off between having too few temperatures' sampling points and compromising rewarming efficiency due to the insertion of temperature sensors. Challenges such as imprecise manufacturing of the rewarming cavity and limited temperature monitoring can hinder enhancements in electromagnetic rewarming. Therefore, a numerical model serves as a valuable tool for optimizing electromagnetic rewarming, from system parameters to selecting CPA solutions, aiming for higher energy utilization and more uniform temperature distribution. This model enables convenient adjustments to various parameters, facilitating improvements in the rewarming process.

In this section, combined numerical and experimental investigation of electromagnetic rewarming for cryopreservation was carried out. The shape of sample was optimized numerically, and a cylindrical sample holder was selected to achieve a high rewarming rate. A variety of CPA solutions' physical properties were experimentally determined and used for the simulation of SMER rewarming. The temperature dependence of complex permittivity and specific heat were determined over the rewarming range. The thermal conductivity is regarded as a constant due to the current limitation of our measurement technique. It would bring large errors in determining the temperature distribution in traditional conductive rewarming simulations (e.g., using water bath heating). However, when the electromagnetic energy serves as the major heating energy source, the heating due to heat conduction within the sample could have less contribution to the temperature change. In future modeling and numerical simulation, thermal conductivity values of the CPA solutions over the entire temperature change range should be determined and used in calculations to achieve more accurate results.

Using high-power electromagnetic energy in the rewarming system requires delicate control. The source power, if not well controlled, can cause damage to the system itself. We observed that in the heating of some CPA solutions with less absorption of the electromagnetic power, the circuits were burned internally by the reflected electromagnetic power, which was supposed to be used for the rewarming of cryopreserved sample. Using numerical simulation can avoid those potential undesired failures and costs. Under the assistance of numerical simulation, higher power can be employed under an optimized condition in the further development of electromagnetic heating systems.

A hybrid rewarming concept was proposed and tested by experiments. It was confirmed that using the hybrid rewarming, the uniformity of the temperature profile was significantly improved. Besides, in a study by Wang et al.,[39] magnetic NPs were added in CPA solutions to enhance the SMER rewarming. The rewarming rate was increased to 47°C/min with a maximum temperature gradient 1.64°C/mm. The rewarming rate is at the same order of magnitude of the current study optimized by the selection of CPA solutions and hybrid rewarming. The final temperature gradient 1.64°C/mm corresponds to a large temperature difference for a sample in a size of > 10 mm in diameter.

Another study evaluated the rewarming with the combination of the SMER heating and water bath.[50] However, the temperature gradient turned out to be 28.7°C/mm, corresponding to over a 200°C temperature difference in the cryopreserved material of a dimension over tens of millimeters. Thus, these methods could hardly be adopted in the tissue/organ preservation currently. The hybrid rewarming design in this study may serve as a more appropriate approach from the perspective of warming uniformity. It should be noted that the central heating rod used in the current hybrid rewarming is inflexible and thick, which cannot be easily employed for organ preservation. A soft material rod with high electromagnetic absorption ability should be selected and used as an auxiliary conduction heat source in the sample holder to facilitate the rewarming process.

Since magnetic NPs presented a significant ability to convert magnetic energy into heat during the SMER rewarming, the impact of the nanoparticle will be further evaluated and optimized.[51–53] In addition, careful research should be conducted to reduce the nanoparticle's concentration by manipulating and optimizing electromagnetic field distribution and increasing magnetic power utilization efficiency. The physical properties of CPA solutions containing the nanoparticle should be determined experimentally in subzero temperature ranges, which may involve phase changes. These determined properties will be used in numerical simulation to optimize the SMER rewarming processes in the presence of the nanoparticles.

6. SMER REWARMING ENHANCEMENT BY USING MAGNETIC NANOPARTICLES

In recent decades, MNPs have significantly impacted various diagnostic and therapeutic fields, including noninvasive magnetic resonance imaging, targeted drug delivery, and hyperthermia therapy.[54–58] Leveraging the heat-generation capability of MNPs under an external oscillating magnetic field, MNP-based hyperthermia can induce localized temperature increases fatal to cancer cells but sparing to normal cells. The innovative integration of a radiofrequency electromagnetic system with MNPs as thermal mediators has expanded from hyperthermia to cryopreservation.[59,60] This advancement aims to mitigate the critical shortage of tissues and organs for transplantation, marking a significant step forward in biomedical applications of MNPs.[61]

In the latest studies,[62] MNPs were introduced to enhance the performance of SMER heating by incorporating low concentrations of 10 or 15 nm iron oxide NPs into the CPA solutions. This approach utilized both electric and magnetic field energy to heat up samples during SMER rewarming, and remarkably achieved an average peak warming rate of $> 200°$C/min for bulk cryopreserved materials, using less EM power compared to radiofrequency coil magnetic rewarming or other EM heating systems. Thermal distribution during rewarming was assessed, and thermal analysis explored the NPs' enhanced effects. The optimized SMER+MNPs system significantly reduced the necessary quantity of NPs to 0.1 mg of Fe per milliliter, presenting a safer option for biological applications compared to higher dosages used in other techniques. This reduction in MNP dosage, coupled with improved heating efficiency, positions this study as a promising approach to address the challenges of tissue and organ preservation rewarming.

6.1 Materials

6.1.1 CPA/Vitrification Solutions

DPVP solution, comprising 5.2 M dimethyl sulfoxide [(DMSO); Sigma-Aldrich, St. Louis, MI], 6% (g/dl) polyvinylpyrrolidone [(PVP); Sigma-Aldrich] in a phosphate buffered saline (PBS) (Sigma-Aldrich) solution, was selected for this study to investigate the N-methylpyrrolidone (NMP) enhancement effect, because its thermal and electric properties have been determined (Section 4) and its demonstrated potential for achieving higher warming rates and reduced temperature gradients in preliminary numerical simulations. For comparative purposes in the freezing/vitrification analysis, a 5.2 M DMSO solution was used. All solutions were prepared a day prior to conducting the cooling and rewarming experiments.

6.1.2 Magnetic Nanoparticles

In this research, the MNPs utilized were 10 and 15 nm iron oxide (Fe_3O_4) NPs with amine groups, in 10 mM PBS (Ocean NanoTech LLC, San Diego, CA). These MNPs were then diluted in CPA solutions, resulting in composite CPA solutions with MNPs concentrations of 0.05, 0.1, and 0.2 mg Fe per milliliter for DPVP solutions. The distribution of the two sizes of MNPs within the DPVP solutions was analyzed using transmission electron microscopy (TEM). Samples of DPVP containing MNPs were prepared on either 200-mesh carbon-coated grids or 300-mesh lacey carbon grids (Electron Microscopy Sciences, Hatfield, PA) and imaged using a Gatan Ultrascan charge-coupled device camera through Digital Micrograph software (Gatan, Pleasanton, CA).

6.2 Methods

6.2.1 Cooling/Vitrification Process

The CPA solutions, totaling 20 mL and contained in a 30 × 100 mm holder, were suspended using an aluminum hook within a liquid nitrogen container, positioned above the liquid nitrogen surface to undergo cooling by vapor phase nitrogen. The cooling rate was approximately determined by adjusting the distance between the CPA solution and the liquid nitrogen surface. Changes in the temperature of the CPA solutions were monitored, allowing for an estimation of the cooling rate for subsequent thermal analysis. Upon reaching –140°C, the CPA solutions were inspected to ascertain whether they had formed a transparent amorphous state or an opaque crystalline solid state.

6.2.2 Temperature Profile Measurement

In Section 5 detailing numerical simulations and the description of the SMER rewarming system, a method for measuring temperature was introduced. To preserve the integrity of the electromagnetic field distribution during rewarming, a fiber-optic sensor connected to a thermometer (Neoptix, Quebec City, Canada) was employed to monitor the CPA solutions' temperature in real time. Once the cryopreserved CPA solutions warmed to 0°C, thereby exiting the critical lethal temperature zone of –60 to –5°C or the devitrification/recrystallization zone, an infrared thermal camera (FLIR, Wilsonville, OR) was utilized to capture the surface thermography of the CPA solutions.

6.2.3 Freezing–Thawing Behavior Characterization and Visualization

Differential scanning calorimetry (Perkin Elmer, Waltham, MA) was utilized to analyze the freezing–thawing behavior and specific heat of sample solutions with varying concentrations of MNPs. An empty pan served as the reference for these measurements. Prior to the experiments, calibrations for temperature and heat flow were performed using n-dodecane and n-octane. For the DSC measurements, 6 μL of each sample solution was sealed in aluminum pans and placed in the DSC apparatus. Each measurement was conducted three times for consistency. To examine freezing–thawing behavior, samples were cooled to –150°C at a rate of 5°C/min, then heated to 20°C at a rate of 100°C/min.

6.2.4 Thermal Conductivity Assessment of the Vitrification Solutions with Nanoparticles

As detailed in Section 4, the CPA solution thermal conductivity measurement system, devised by Liang et al.,[32] integrates a digital multimeter (Keithley, Cleveland, OH), a microfabricated thermal sensor, and a data acquisition computer. Employing the transient hot wire principle, this compact device features a protective $SiO_2/Au/SiO_2$ layered structure encompassing a serpentine gold coil, which serves both as a heater and a passive thermometer. Demonstrated to provide high accuracy, consistency, and reliability, this sensor has been successfully used to assess the thermal conductivity of biomaterials and solutions, including vitrification solutions with varying nanoparticle concentrations. Measurements were conducted thrice across a temperature range from –30 to 20°C.

6.2.5 Statistical Analysis

The statistical analysis was carried out using R (version 3.2.4). The data were presented as mean value plus or minus the standard deviation. Differences of $p < 0.05$ were considered to be of statistical significance.

6.3 Results

6.3.1 MNPs Dispersion in CPA/Vitrification Solution

In the realm of MNP-based radio-frequency (RF) heating for biomedical applications, it has been observed that nanoparticle aggregation can impede the conversion of electromagnetic energies into heat, underscoring the importance of preventing such aggregation for efficient magnetic heat induction.[60,63] Consequently, assessing the distribution of MNPs within the CPA solution beforehand is crucial. Figure 15(a) displays CPA solutions containing either 10 or 15 nm iron oxide NPs at concentrations of 0, 0.05, and 0.2 mg Fe mL^{-1}, respectively. These solutions were subjected to a freezing process down to –80°C, stored in a –80°C freezer for at least one day, and then thawed. Unlike in other CPA solutions where iron oxide NPs were added, no visible clusters or stratification of NPs were observed. TEM images [Fig. 15(b)] confirm that at the low concentrations utilized, NPs remained well-dispersed without significant aggregation, which is preferable for interaction with the electromagnetic field and could help minimize potential inhomogeneity due to large nanoparticle aggregates during electromagnetic rewarming.

6.3.2 Vitrification

The critical cooling rate for DPVP, defined as the minimum rate necessary to prevent significant ice formation, was found to be $< 10°C/min$.[64,65] During the cooling process, DPVP was cooled slowly but at a rate exceeding the CCR, as illustrated in Fig. 16(a). To alleviate residual thermal stress that could lead to devitrification, an annealing step was introduced immediately after reaching the glass transition temperature. As shown in Fig. 16(b), this method of vapor phase nitrogen cooling resulted in the formation of transparent solids at –140°C for all DPVP solutions with varying nanoparticle concentrations tested in this study. In contrast, using lower concentration CPAs (5.2 M DMSO, for instance) and slow cooling to –140°C led to the formation of opaque crystalline solids. Typically, vitrification of small-volume biomaterials with lower concentrations of CPAs needs

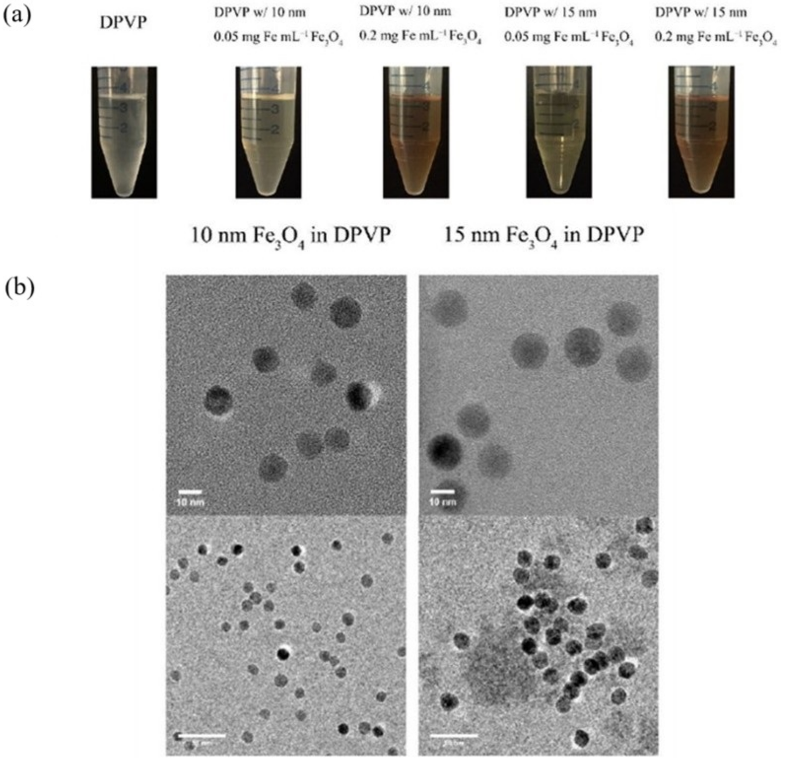

FIG. 15: DPVP solutions with 10, 15 nm Fe_3O_4 NPs: (a) visual examination of solutions with or without different concentration NPs after slow cooling and rapid rewarming and (b) transmission electron microscopy images. Stratified solutions after rewarming or nanoparticle aggregations were not observed.

ultrarapid cooling, often achieved by direct immersion in liquid nitrogen. However, achieving both rapid and uniform cooling for larger biomaterials is challenging. The nonuniform temperature profiles during the rapid cooling process can cause high thermal stress and fracture in the cryopreserved biomaterials. As can be seen in Fig. 16(b), substantial ice crystals were observed around the fracture planes in the CPA solutions plunged into liquid nitrogen for a fast cooling rather than slowly cooled by vapor phase nitrogen avoiding the fracture otherwise.

6.3.3 Effects of MNPs on Warming Rate and Uniformity during SMER Rewarming Processes

Following the cooling by vapor phase nitrogen, as previously described, the samples were insulated with Styrofoam to minimize the effects of natural convection heat transfer. They were then positioned at the center of the resonance chamber and subjected to rewarming by the SMER system. Temperature changes of DPVP samples containing various

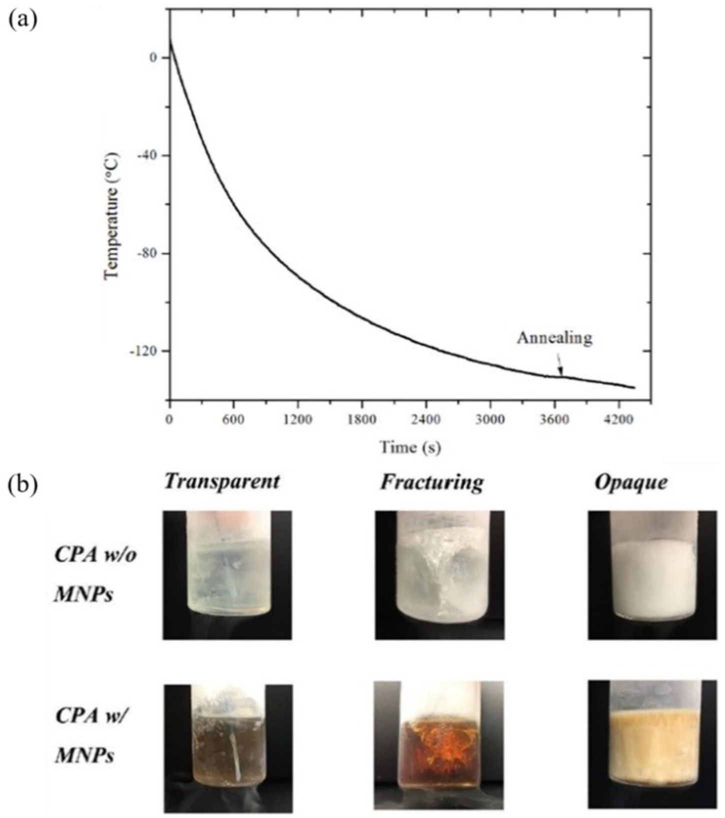

FIG. 16: (a) A representative temperature change is illustrated using the vapor phase cooling method recorded by thermal sensors. (b) Typical visual images of CPA solutions cooled down to –140°C. DPVP with or without Fe_3O_4 NPs formed transparent solid (left) using the vapor phase cooling method. Cracks/fractures (middle) were seen after plunging the bulk DPVP with or without NPs into liquid nitrogen. Opaque crystalline solid (right) were observed for slowly cooled 5.2 M DMSO solution. Apparently, 5.2 M DMSO is insufficient to achieve vitrification at this low cooling rate. (Reprinted with permission from the American Chemical Society, Copyright 2019.)[62]

concentrations of 10 and 15 nm MNPs were recorded from –130 to 0°C by using fiber-optic thermometers during the SMER rewarming processes.

For large tissue cryopreservation, a relatively slow initial warming rate is recommended to prevent fractures or cracks caused by nonuniform warming, followed by rapid warming to navigate through the recrystallization zone swiftly. The last decade saw the proposal of an ice-free cryopreservation protocol for tissue preservation, utilizing CPA solutions at concentrations high enough for vitrification but storing cryopreserved tissues above the glass transition temperature (around –80°C).[66,67] Consequently, in this study, the rewarming process was divided into two phases: –130 to –70°C and –70 to 0°C, with corresponding average rewarming rates reported in Figs. 17(a) and 17(b).

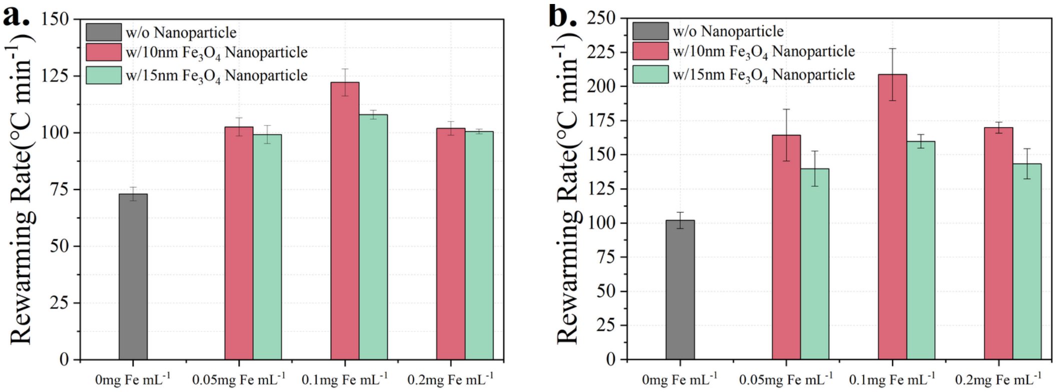

FIG. 17: (a) Average warming rates were determined for the rewarming temperature range –130 to –70°C. (b) Average warming rates were determined for the rewarming temperature range –70 to 0°C. (The average rewarming rate was calculated as the difference between the initial temperature and final temperature, divided by the time.)

The emphasis was placed on accelerating the rewarming process within the critical temperature range of –70 to 0°C, a zone particularly risky for cryopreserved materials. Using the SMER system, DPVP without MNPs achieved an average rewarming rate of 76.0 ± 1.5°C/min from –130 to –70°C, and 105.6 ± 6.0°C/min from –70 to 0°C. To investigate the impact of NPs of different sizes, 10 and 15 nm Fe_3O_4 NPs were added since the MNPs exhibit superparamagnetic properties with size reduced to $\sim$ 15 nm.[68] Superparamagnetic MNPs possess remarkable heating capabilities at lower magnetic fields.[69]

Incorporating MNPs at a concentration of 0.05 mg Fe mL^{-1} (a lowest concentration in the study), increased the rewarming rates to 104.9 ± 2.9 and 101.9 ± 4.3°C/min for 10 and 15 nm NPs, respectively, in the –130 to –70°C range. For the –70 to 0°C range, rewarming rates rose to 164.4 ± 22.6 and 142.3 ± 12.3°C/min for 10 and 15 nm NPs, marking a 61.2 and 39.6% enhancement in rewarming rates. Figures 18(a) and 18(b) present the warming behavior of CPA solutions via DSC, with cooling and heating rates set to align with those of bulk materials rewarming in the SMER system. The inclusion of MNPs did not alter the heat flow during rewarming. Furthermore, a warming rate at 100°C/min prevented devitrification in DPVP, with or without MNPs, confirming that fast rewarming rates ($>$ 100°C/min) generated by the SMER system can effectively prevent the devitrification or recrystallization.

Considering the dynamic interplay between oscillating magnetic fields and MNPs, the ideal nanoparticle size varies across biomedical applications. In hyperthermia studies using RF coils, it is noted that MNP heating efficiency is size-dependent due to variations in electromagnetic field frequency, intensity, and distribution patterns. Additionally, MNP magnetization, which influences heating, varies with temperature and is supported by experimental findings. This suggests that the heating enhancement by MNPs in cryopreservation, which can extend to temperatures as low as –196°C, differs fundamentally from

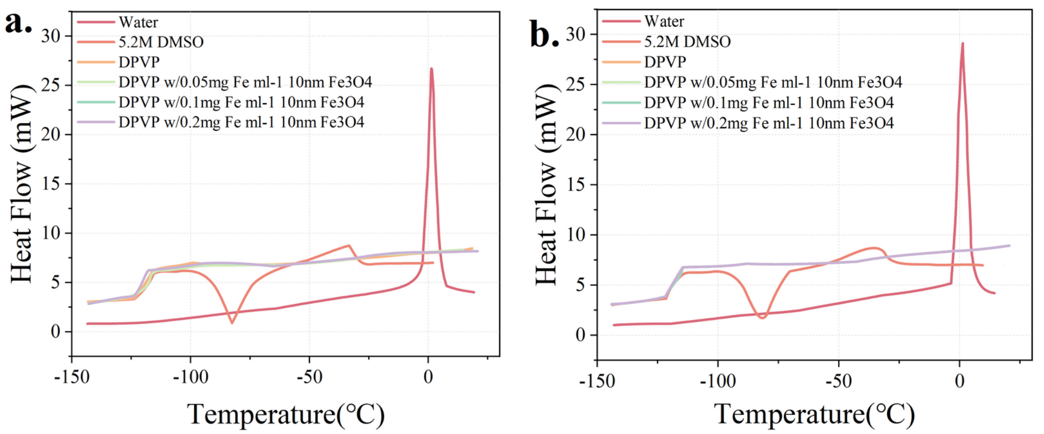

FIG. 18: Warming behavior of CPA solutions with (a) 10 nm MNPs and (b) 15 nm MNPs. The devitrification and melting of 5.2 M DMSO occurred at a warming rate 100°C/min, whereas the apparent recrystallization of DPVP with or without MNPs was not observed using the same warming process. The cooling and heating rates were set in accordance with the bulk cryopreserved materials in the SMER rewarming.

applications like magnetic hyperthermia, where the temperature is $\sim$ 40°C. In this research, at cryogenic temperatures, the SMER system operates within a different frequency range (hundreds of megahertz versus hundreds of kilohertz) and exhibits a unique electromagnetic field distribution compared to radiofrequency heating devices used in hyperthermia or nanowarming. Therefore, optimal magnetic nanoparticle sizes for maximal magnetic energy absorption in the cryogenic temperature range need to be further investigated and determined.

Figure 17(b) demonstrates that DPVP containing 10 nm Fe_3O_4 NPs achieved higher rewarming rates compared to those with 15 nm MNPs when rewarmed by SMER system. Specifically, at a concentration of 0.05 mg Fe mL^{-1}, the rewarming rates were 164.4 ± 22.6°C/min for 10 nm MNPs versus 142.3 ± 12.33°C/min for 15 nm MNPs (difference not statistically significant, $p = 0.15$). At 0.1 mg Fe mL^{-1}, the rates were 210.1 ± 19.7°C/min for 10 nm MNPs versus 162.4 ± 3.7°C/min for 15 nm MNPs ($p < 0.05$), and at 0.2 mg Fe mL^{-1}, they were 171.4 ± 2.7°C/min for 10 nm MNPs versus 145.3 ± 11.0°C/min for 15 nm MNPs ($p < 0.05$), across the temperature range of –70 to 0°C. These findings suggest that 10 nm iron oxide NPs are more effective for electromagnetic energy absorption during the SMER warming processes.

Figure 17(b) also illustrates the influence of nanoparticle concentration on the rewarming rate for both 10 and 15 nm MNPs (Fe_3O_4). For DPVP solutions containing 10 nm MNPs, the optimal rewarming rate of 210.1 ± 19.7°C/min was achieved at a concentration of 0.1 mg Fe mL^{-1}, significantly surpassing the rates at lower (0.05 mg Fe mL^{-1}) and higher (0.2 mg Fe mL^{-1}) concentrations ($p < 0.05$). A similar trend was observed for 15 nm MNPs, where the highest rewarming rate was also found at 0.1 mg Fe mL^{-1}, indicating that rewarming rates do not necessarily increase with higher MNPs concentrations. The use of a small and effective concentration of MNPs is advantageous to minimize potential risks associated with excessive MNPs dosages.

The abovementioned findings also suggest a possible collective behavior among MNPs at increased concentrations, which does not correspond to a greater efficiency in converting electromagnetic energy to heat during SMER rewarming. The interaction between more concentrated NPs and potential ice recrystallization might impede heating efficiency. Furthermore, the specific impact of increased interparticle interactions on heating efficiency remains unclear, with some studies indicating a decrease in heating efficiency with higher MNP concentrations,[70–72] while others reported the opposite.[73,74] The Gao et al.[75] study suggested that the nonlinear increase in rewarming with the concentration of MNPs may be attributed to the issue of nanoparticle aggregation. These findings highlight the need for further research to understand the electromagnetic energy conversion as a function of low temperature and specific frequency.

7. CONCLUSION

This chapter introduces a study of the SMER technology to achieve optimal rapid-and-uniform rewarming of large cryopreserved biomaterials, an increased and urgent need in cryopreservation of tissues and organs. SMER offers a solution by enabling volumetric heating, bypassing the limitations of conventional heating methods that cannot produce rapid-and-uniform warming and may induce lethal ice-recrystallization and high thermal stress damage to cells and tissues. Coupled with SMER technology development, this study also evaluated various vitrification solutions' ability and physical properties to convert electromagnetic energy into heat. The DPVP solution emerged as a promising candidate due to its effective energy conversion ability and favorable thermal properties. Through experimental analysis and numerical simulations, this study evaluated the potential for rapid warming rates and the risk of "thermal runaway," proposing a concept that combines electromagnetic and conductive (hybrid) rewarming. Research results highlighted the enhanced rewarming efficiency and temperature uniformity achieved by using low concentrations of MNPs, suggesting the existence of an optimal nanoparticle concentration for best rewarming outcomes. The research findings contribute to further optimizing SMER system with implications for more efficient and safer cryopreservation practices.

On the basis of Maxwell theory, the SMER rewarming system can be scaled up and down to achieve rapid-and-uniform rewarming of different sizes/volumes of biospecimens (including tissues, organs, and larger cell suspensions). This advancement also requires enhancements in the microwave power and control system coupled with SMER technology. Presently, comprehensive data of thermal and electromagnetic properties of CPA/vitrification solutions at cryogenic temperatures remain scarce, yet such knowledge is crucial for optimizing the CPA/vitrification solutions for both cooling and warming processes. Moreover, the interaction mechanisms of MNPs within alternating electric and magnetic fields require deeper exploration. Overall, the SMER heating system emerges and is approved as a very promising technology to achieve optimal rewarming of large, cryopreserved, living biomaterials.

REFERENCES

1. Jang, T.H., Park, S.C., Yang, J.H., Kim, J.Y., Seok, J.H., Park, U.S., Choi, C.W., Lee, S.R., and Han, J., Cryopreservation and Its Clinical Applications, *Integ. Med. Res.*, vol. **6**, no. 1, pp. 12–18, 2017.
2. Kuleshova, L.L., Gouk, S.S., and Hutmacher, D.W., Vitrification as a Prospect for Cryopreservation of Tissue-Engineered Constructs, *Biomaterials*, vol. **28**, no. 9, pp. 1585–1596, 2007.
3. Mazur, P., Cryobiology: The Freezing of Biological Systems, *Science*, vol. **168**, no. 3934, pp. 939–949, 1970.
4. Han, Z., Rao, J.S., Gangwar, L., Namsrai, B.-E., Pasek-Allen, J.L., Etheridge, M.L., Wolf, S.M., Pruett, T.L., Bischof, J.C., and Finger, E.B., Vitrification and Nanowarming Enable Long-Term Organ Cryopreservation and Life-Sustaining Kidney Transplantation in a Rat Model, *Nat. Commun.*, vol. **14**, no. 1, p. 3407, 2023.
5. Sharma, A., Lee, C.Y., Namsrai, B.-E., Han, Z., Tobolt, D., Rao, J.S., Gao, Z., Etheridge, M.L., Garwood, M., Clemens, M.G., Bischof, J.C., and Finger, E.B., Cryopreservation of Whole Rat Livers by Vitrification and Nanowarming, *Annals Biomed. Eng.*, vol. **51**, no. 3, pp. 566–577, 2023.
6. Chiu-Lam, A., Staples, E., Pepine, C.J., and Rinaldi, C., Perfusion, Cryopreservation, and Nanowarming of Whole Hearts Using Colloidally Stable Magnetic Cryopreservation Agent Solutions, *Sci. Adv.*, vol. **7**, no. 2, p. eabe3005, 2021.
7. Vollmer, M., Physics of the Microwave Oven, *Phys. Ed.*, vol. **39**, no. 1, pp. 74–81, 2004.
8. Allen, J. and Ketterer, F.D., Analytical Investigation of Thermal Runaway during Electrical Thawing of Frozen Tissue, *Cryobiology*, vol. **4**, no. 5, p. 248, 1968.
9. Ketterer, F.D., Holst, H.I., and Lehr, H.B., Improved Viability of Kidneys with Microwave Thawing, *Cryobiology*, vol. **8**, p. 395, 1971.
10. Guttman, F.M., Lizin, J., Robitaille, P., Blanchard, H., and Turgeon-Knaack, C., Survival of Canine Kidneys after Treatment with Dimethyl-Sulfoxide, Freezing at –80°C, and Thawing by Microwave Illumination, *Cryobiology*, vol. **14**, no. 5, pp. 559–567, 1977.
11. Pegg, D.E., Green, C.J., and Walter, C.A., Attempted Canine Renal Cryopreservation Using Dimethyl Sulphoxide Helium Perfusion and Microwave Thawing, *Cryobiology*, vol. **15**, no. 6, pp. 618–626, 1978.
12. Burdette, E.C., Karow, A.M., and Jeske, A.H., Design, Development, and Performance of an Electromagnetic Illumination System for Thawing Cryopreserved Kidneys of Rabbits and Dogs, *Cryobiology*, vol. **15**, no. 2, pp. 152–167, 1978.
13. Pozar, D.M., *Microwave Engineering*, 4th ed., Chichester, UK: Wiley, 2012.
14. Rachman, M.J., Evans, S., and Pegg, D.E., Experimental Results on the Rewarming of a Cryopreserved Organ Phantom in a UHF Field, *J. Biomed. Eng.*, vol. **14**, no. 5, pp. 397–403, 1992.
15. Robinson, M.P. and Pegg, D.E., Rapid Electromagnetic Warming of Cells and Tissues, *IEEE Trans. Biomed. Eng.*, vol. **46**, no. 12, pp. 1413–1425, 1999.
16. Cai-Cheng, L., Huai-Zhi, L., and Dayong, G., Combined Electromagnetic and Heat-Conduction Analysis of Rapid Rewarming of Cryopreserved Tissues, *IEEE Trans. Microwave Theor. Tech.*, vol. **48**, no. 11, pp. 2185–2190, 2000.

17. Luo, D., Yu, C., He, L., Lu, C., and Gao, D., Development of a Single Mode Electromagnetic Resonant Cavity for Rewarming of Cryopreserved Biomaterials, *Cryobiology*, vol. **53**, no. 2, pp. 288–293, 2006.
18. Shen, R., Zhiquan, S., Jiaji, P., Ji, P., Junlan, W., Chunhua, Z., and Dayong, G., Development of a Novel Electromagnetic Rewarming Technology for the Cryopreservation of Stem Cells with Large Volume, *Novel Perspectives of Stem Cell Manufacturing and Therapies*, K. Diana, and M. Ana Colette, Eds., Rijeka, Croatia: IntechOpen, 2020.
19. Shen, R., Shu, Z., Wang, Z., Jin, Y., Ma, R., Hao, S., Yang, X., and Gao, D., Successful Vitreous Cryopreservation of Rabbit Jugular Vein Using Magnetic Nanoparticles Enhanced Single_mode Electromagnetic Resonance Rewarming System, *Cryobiology*, vol. **103**, pp. 173–174, 2021.
20. Ren, S.A.-O., Shu, Z., Pan, J., Wang, Z.A.-O., Ma, R.A.-O., Peng, J., Chen, M., and Gao, D., Single-Mode Electromagnetic Resonance Rewarming for the Cryopreservation of Samples with Large Volumes: A Numerical and Experimental Study, *Biopreserv. Biobank.*, vol. **20**, no. 4, pp. 317–322, 2022.
21. Wang, Z., Ren, S., Shu, Z., Ma, R., and Gao, D., Screening and Optimization of Cryoprotective Agents (CPAs) for Electromagnetic Heating of Cryopreserved Biomaterials, *Cryobiology*, vol. **109**, p. 16, 2022.
22. Robinson, M.P., Wusteman, M.C., Wang, L., and Pegg, D.E., Electromagnetic Re-Warming of Cryopreserved Tissues: Effect of Choice of Cryoprotectant and Sample Shape on Uniformity of Heating, *Phys. Med. Biol.*, vol. **47**, no. 13, pp. 2311–2325, 2002.
23. Wusteman, M.C., Pegg, D.E., Robinson, M.P., Wang, L.-H., and Fitch, P., Vitrification Media: Toxicity, Permeability, and Dielectric Properties, *Cryobiology*, vol. **44**, no. 1, pp. 24–37, 2002.
24. Eisenberg, D.P., Taylor, M.J., and Rabin, Y., Thermal Expansion of the Cryoprotectant Cocktail DP6 Combined with Synthetic Ice Modulators in Presence and Absence of Biological Tissues, *Cryobiology*, vol. **65**, no. 2, pp. 117–125, 2012.
25. Hunt, C.J., Song, Y.C., Bateson, E.A.J., and Pegg, D.E., Fractures in Cryopreserved Arteries, *Cryobiology*, vol. **31**, no. 5, pp. 506–515, 1994.
26. Ansorge, S., Esteban, G., and Schmid, G., Multifrequency Permittivity Measurements Enable On-Line Monitoring of Changes in Intracellular Conductivity Due to Nutrient Limitations during Batch Cultivations of CHO Cells, *Biotechnol. Prog.*, vol. **26**, no. 1, pp. 272–283, 2010.
27. Juan-Garca, P. and Torrents, J.M., Measurement of Mortar Permittivity during Setting Using a Coplanar Waveguide, *Meas. Sci. Technol.*, vol. **21**, no. 4, p. 045702, 2010.
28. Lee, K.Y., Abbas, Z., Yeow, Y.K., Nur Sharizan, M.D., and Meng, C.E., *In Situ* Measurements of Complex Permittivity and Moisture Content in Oil Palm Fruits, *Eur. Phys. J. Appl. Phys.*, vol. **49**, no. 3, p. 31201, 2010.
29. Waldron, R.A., Perturbation Theory of Resonant Cavities, *Proc. IEE Part C: Monographs*, vol. **107**, no. 12, p. 272, 1960.
30. Ren, S., Shu, Z., Pan, J., Peng, J., Wang, J., Zhao, C., and Gao, D., Development of a Novel Electromagnetic Rewarming Technology for the Cryopreservation of Stem Cells with Large Volume, *Novel Perspectives of Stem Cell Manufacturing and Therapies*, London: IntechOpen, 2021.
31. Pan, J., Shu, Z., Ren, S., and Gao, D., Determination of Dielectric Properties of Cryoprotective

Agent Solutions with a Resonant Cavity for the Electromagnetic Rewarming in Cryopreservation, *Biopreserv. Biobank*., vol. **15**, no. 5, pp. 404–409, 2017.

32. Liang, X.M., Sekar, P.K., Zhao, G., Zhou, X., Shu, Z., Huang, Z., Ding, W., Zhang, Q., and Gao, D., High Accuracy Thermal Conductivity Measurement of Aqueous Cryoprotective Agents and Semi-Rigid Biological Tissues Using a Microfabricated Thermal Sensor, *Sci. Rep*., vol. **5**, no. 1, p. 10377, 2015.
33. Pan, J., Shu, Z., Zhao, G., Ding, W., Ren, S., Sekar, P.K., Peng, J., Kramlich, J., Chen, M., and Gao, D., Towards Uniform and Fast Rewarming for Cryopreservation with Electromagnetic Resonance Cavity: Numerical Simulation and Experimental Investigation, *Appl. Therm. Eng*., vol. **140**, pp. 787–798, 2018.
34. Ehrlich, L.E., Feig, J.S.G., Schiffres, S.N., Malen, J.A., and Rabin, Y., Large Thermal Conductivity Differences between the Crystalline and Vitrified States of DMSO with Applications to Cryopreservation, *Plos One*, vol. **10**, no. 5, p. e0125862, 2015.
35. Gao, D. and Critser, J.K., Mechanisms of Cryoinjury in Living Cells, *ILAR J*., vol. **41**, no. 4, pp. 187–196, 2000.
36. Bai, X., Pegg, D.E., Evans, S., and Penfold, J.D.J., Analysis of Electromagnetic Heating Patterns inside a Cryopreserved Organ, *J. Biomed. Eng*., vol. **14**, no. 6, pp. 459–466, 1992.
37. Penfold, J.D.J. and Evans, S., Control of Thermal Runaway and Uniformity of Heating in the Electromagnetic Rewarming of a Cryopreserved Kidney Phantom, *Cryobiology*, vol. **30**, no. 5, pp. 493–508, 1993.
38. Han, X., Gao, D.Y., Luo, D., Yu, C., and Lu, C.C., Numerical Simulation of the Microwave Rewarming Process of Cryopreserved Organs, *Microwave Opt. Technol. Lett*., vol. **46**, no. 3, pp. 201–205, 2005.
39. Wang, T., Zhao, G., Liang, X.M., Xu, Y., Li, Y., Tang, H., Jiang, R., and Gao, D., Numerical Simulation of the Effect of Superparamagnetic Nanoparticles on Microwave Rewarming of Cryopreserved Tissues, *Cryobiology*, vol. **68**, no. 2, pp. 234–243, 2014.
40. Ma, L., Paul, D.L., Pothecary, N.M., Railton, C.J., Bows, J., Barratt, L., Mullin, J., and Simons, D., Experimental Validation of a Combined Electromagnetic and Thermal FDTD Model of a Microwave Heating Process, *IEEE Trans. Microwave Theor. Tech.*, vol. **43**, no. 11, pp. 2565–2572, 1995.
41. Torres, F. and Jecko, B., Complete FDTD Analysis of Microwave Heating Processes in Frequency-Dependent and Temperature-Dependent Media, *IEEE Trans. Microwave Theory Tech.*, vol. **45**, no. 1, pp. 108–117, 1997.
42. Pathak, V., Yun, Z., and Iskander, M.F., Development of an Integrated Multi-Grid 3D FDTD and Finite-Difference Heat Transfer Code to Simulate Microwave Drying in Multimode Cavities, *IEEE Antennas and Propagation Society Int. Symp*., Boston, MA, pp. 138–141, 2001.
43. Zhang, Q., Jackson, T.H., and Ungan, A., Numerical Modeling of Microwave Induced Natural Convection, *Int. J. Heat Mass Transf*., vol. **43**, no. 12, pp. 2141–2154, 2000.
44. Michael, V., Physics of the Microwave Oven, *Phys. Ed*., vol. **39**, no. 1, p. 74, 2004.
45. Basak, T., Aparna, K., Meenakshi, A., and Balakrishnan, A.R., Effect of Ceramic Supports on Microwave Processing of Porous Food Samples, *Int. J. Heat Mass Transf*., vol. **49**, no. 23, pp. 4325–4339, 2006.
46. Zhang, H., Datta, A.K., Taub, I.A., and Doona, C., Electromagnetics, Heat Transfer, and Thermokinetics in Microwave Sterilization, *AIChE J*., vol. **47**, no. 9, pp. 1957–1968, 2001.

47. Evans, S., Rachman, M.J., and Pegg, D.E., Design of a UHF Applicator for Rewarming of Cryopreserved Biomaterials, *IEEE Trans. Biomed. Eng*., vol. **39**, no. 3, pp. 217–225, 1992.
48. Farag, S., Sobhy, A., Akyel, C., Doucet, J., and Chaouki, J., Temperature Profile Prediction within Selected Materials Heated by Microwaves at 2.45 GHz, *Appl. Therm. Eng*., vol. **36**, pp. 360–369, 2012.
49. Lu, C.-C., Li, H.-Z., and Gao, D., Combined Electromagnetic and Heat-Conduction Analysis of Rapid Rewarming of Cryopreserved Tissues, *IEEE Trans. Microwave Theory Tech*., vol. **48**, no. 11, pp. 2185–2190, 2000.
50. Wang, T., Zhao, G., Deng, Z., Gao, C., Cao, Y., and Gao, D., Theoretical Investigation of a Novel Microwave Antenna Aided Cryovial for Rapid and Uniform Rewarming of Frozen Cryoprotective Agent Solutions, *Appl. Therm. Eng*., vol. **89**, pp. 968–977, 2015.
51. Etheridge, M.L., Xu, Y., Rott, L., Choi, J., Glasmacher, B., and Bischof, J.C., RF Heating of Magnetic Nanoparticles Improves the Thawing of Cryopreserved Biomaterials, *Technology (Singapore)*, vol. **2**, no. 3, pp. 229–242, 2014.
52. Lv, Y.-G., Deng, Z.-S., and Liu, J., 3-D Numerical Study on the Induced Heating Effects of Embedded Micro/Nanoparticles on Human Body Subject to External Medical Electromagnetic Field, *IEEE Trans. Nanobiosci*., vol. **4**, no. 4, pp. 284–294, 2005.
53. Wang, J., Zhao, G., Zhang, Z., Xu, X., and He, X., Magnetic Induction Heating of Superparamagnetic Nanoparticles during Rewarming Augments the Recovery of hUCM-MSCs Cryopreserved by Vitrification, *Acta Biomater*., vol. **33**, pp. 264–274, 2016.
54. Hayashi, K., Ono, K., Suzuki, H., Sawada, M., Moriya, M., Sakamoto, W., and Yogo, T., High-Frequency, Magnetic-Field-Responsive Drug Release from Magnetic Nanoparticle/Organic Hybrid Based on Hyperthermic Effect, *ACS Appl. Mater. Interfaces*, vol. **2**, no. 7, pp. 1903–1911, 2010.
55. Kumar, C.S.S.R. and Mohammad, F., Magnetic Nanomaterials for Hyperthermia-Based Therapy and Controlled Drug Delivery, *Adv. Drug Del. Rev*., vol. **63**, no. 9, pp. 789–808, 2011.
56. Liong, M., Lu, J., Kovochich, M., Xia, T., Ruehm, S.G., Nel, A.E., Tamanoi, F., and Zink, J.I., Multifunctional Inorganic Nanoparticles for Imaging, Targeting, and Drug Delivery, *ACS Nano*, vol. **2**, no. 5, pp. 889–896, 2008.
57. Sun, C., Lee, J.S.H., and Zhang, M., Magnetic Nanoparticles in MR Imaging and Drug Delivery, *Adv. Drug Del. Rev*., vol. **60**, no. 11, pp. 1252–1265, 2008.
58. Park, J.-H., von Maltzahn, G., Xu, M.J., Fogal, V., Kotamraju, V.R., Ruoslahti, E., Bhatia, S.N., Sailor, M.J., and Davis, M.E., Cooperative Nanomaterial System to Sensitize, Target, and Treat Tumors, *Proc. Natl. Acad. Sci*., vol. **107**, no. 3, pp. 981–986, 2010.
59. Sharma, A., Rao, J.S., Han, Z., Gangwar, L., Namsrai, B., Gao, Z., Ring, H.L., Magnuson, E., Etheridge, M., Wowk, B., Fahy, G.M., Garwood, M., Finger, E.B., and Bischof, J.C., Vitrification and Nanowarming of Kidneys, *Adv. Sci*., vol. **8**, no. 19, p. 2101691, 2021.
60. Manuchehrabadi, N., Gao, Z., Zhang, J., Ring, H.L., Shao, Q., Liu, F., McDermott, M., Fok, A., Rabin, Y., Brockbank, K.G.M., Garwood, M., Haynes, C.L., and Bischof, J.C., Improved Tissue Cryopreservation Using Inductive Heating of Magnetic Nanoparticles, *Sci. Translat. Med*., vol. **9**, no. 379, p. eaah4586, 2017.
61. Giwa, S., Lewis, J.K., Alvarez, L., Langer, R., Roth, A.E., Church, G.M., Markmann, J.F., Sachs, D.H., Chandraker, A., Wertheim, J.A., Rothblatt, M., Boyden, E.S., Eidbo, E., Lee, W.P.A., Pomahac, B., Brandacher, G., Weinstock, D.M., Elliott, G., Nelson, D.,

Acker, J.P., Uygun, K., Schmalz, B., Weegman, B.P., Tocchio, A., Fahy, G.M., Storey, K.B., Rubinsky, B., Bischof, J., Elliott, J.A.W., Woodruff, T.K., Morris, G.J., Demirci, U., Brockbank, K.G.M., Woods, E.J., Ben, R.N., Baust, J.G., Gao, D., Fuller, B., Rabin, Y., Kravitz, D.C., Taylor, M.J., and Toner, M., The Promise of Organ and Tissue Preservation to Transform Medicine, *Nat. Biotechnol.*, vol. **35**, no. 6, pp. 530–542, 2017.

62. Pan, J., Ren, S., Sekar, P.K., Peng, J., Shu, Z., Zhao, G., Ding, W., Chen, M., and Gao, D., Investigation of Electromagnetic Resonance Rewarming Enhanced by Magnetic Nanoparticles for Cryopreservation, *Langmuir*, vol. **35**, no. 23, pp. 7560–7570, 2019.

63. Jeon, S., Hurley, K.R., Bischof, J.C., Haynes, C.L., and Hogan, C.J., Quantifying Intra- and Extracellular Aggregation of Iron Oxide Nanoparticles and Its Influence on Specific Absorption Rate, *Nanoscale*, vol. **8**, no. 35, pp. 16053–16064, 2016.

64. Boutron, P. and Kaufmann, A., Stability of the Amorphous State in the System Water-Glycerol-Dimethylsulfoxide, *Cryobiology*, vol. **15**, no. 1, pp. 93–108, 1978.

65. Fahy, G.M., Wowk, B., Wu, J., and Paynter, S., Improved Vitrification Solutions Based on the Predictability of Vitrification Solution Toxicity, *Cryobiology*, vol. **48**, no. 1, pp. 22–35, 2004.

66. Brockbank, K.G.M.P., Wright, G.J.B.S., Yao, H.P., Greene, E.D.L., Chen, Z.Z.M.S, and Schenke-Layland, K.P., Allogeneic Heart Valve Storage above the Glass Transition at –80°C, *Ann. Thorac. Surg.*, vol. **91**, no. 6, pp. 1829–1835, 2011.

67. Lisy, M., Pennecke, J., Brockbank, K.G.M., Fritze, O., Schleicher, M., Schenke-Layland K., Kaulitz, R., Riemann, I., Weber, C.N., Braun, J., Mueller, K.E., Fend, F., Scheunert, T., Gruber, A.D., Albes, J.M., Huber, A.J., and Stock, U.A., The Performance of Ice-Free Cryopreserved Heart Valve Allografts in an Orthotopic Pulmonary Sheep Model, *Biomaterials*, vol. **31**, no. 20, pp. 5306–5311, 2010.

68. Deatsch, A.E. and Evans, B.A., Heating Efficiency in Magnetic Nanoparticle Hyperthermia, *J. Magn. Magn. Mater.*, vol. **354**, pp. 163–172, 2014.

69. Pankhurst, Q.A., Connolly, J., Jones, S.K., and Dobson, J., Applications of Magnetic Nanoparticles in Biomedicine, *J. Phys. D: Appl. Phys.*, vol. **36**, no. 13, pp. R167–R181, 2003.

70. Piñeiro-Redondo, Y., Bañobre-López, M., Pardiñas-Blanco, I., Goya, G., López-Quintela, M.A., and Rivas, J., The Influence of Colloidal Parameters on the Specific Power Absorption of PAA-Coated Magnetite Nanoparticles, *Nanoscale Res. Lett.*, vol. **6**, no. 1, p. 383, 2011.

71. Wang, X., Gu, H., and Yang, Z., The Heating Effect of Magnetic Fluids in an Alternating Magnetic Field, *J. Magn. Magn. Mater.*, vol. **293**, no. 1, pp. 334–340, 2005.

72. Urtizberea, A., Natividad, E., Arizaga, A., Castro, M., and Mediano, A., Specific Absorption Rates and Magnetic Properties of Ferrofluids with Interaction Effects at Low Concentrations, *J. Phys. Chem. C*, vol. **114**, no. 11, pp. 4916–4922, 2010.

73. Dennis, C.L., Jackson, A.J., Borchers, J.A., Ivkov, R., Foreman, A.R., Lau, J.W., Goernitz, E., and Gruettner, C., The Influence of Collective Behavior on the Magnetic and Heating Properties of Iron Oxide Nanoparticles, *J. Appl. Phys.*, vol. **103**, no. 7, p. 07A319-07A-3, 2008.

74. Andrés Vergés, M., Costo, R., Roca, A.G., Marco, J.F., Goya, G.F., Serna, C.J., and Morales, M.P., Uniform and Water Stable Magnetite Nanoparticles with Diameters around the Monodomain–Multidomain Limit, *J. Phys. D: Appl. Phys.*, vol. **41**, no. 13, p. 134003, 2008.

75. Gao, Z., Ring, H.L., Sharma, A., Namsrai, B., Tran, N., Finger, E.B., Garwood, M., Haynes, C.L., and Bischof, J.C., Preparation of Scalable Silica-Coated Iron Oxide Nanoparticles for Nanowarming, *Adv. Sci.*, vol. **7**, no. 4, p. 1901624, 2020.